# Real-time fault-tolerant moving horizon air data estimation for the RECONFIGURE benchmark

Wan, Yiming; Keviczky, Tamas

**DOI**
10.1109/TCST.2018.2804332

**Publication date**
2018

**Document Version**
Final published version

**Published in**
IEEE Transactions on Control Systems Technology

# Real-Time Fault-Tolerant Moving Horizon Air Data Estimation for the RECONFIGURE Benchmark

Yiming Wan and Tamás Keviczky

***Abstract*— This paper proposes a real-time fault-tolerant estimation approach for combined sensor fault diagnosis and air data reconstruction. Due to simultaneous influence of winds and latent faults on monitored sensors, it is challenging to address the tradeoff between robustness to wind disturbances and sensitivity to sensor faults. As opposed to conventional fault-tolerant estimators that do not consider any constraints, we propose a constrained fault-tolerant estimator using moving horizon estimation (MHE). By exploiting wind bounds according to the weather or flight conditions, this approach improves fault sensitivity without sacrificing disturbance robustness. This improvement is attributed to active inequality constraints caused by faults, as shown in sensitivity analysis of the formulated MHE problem. The challenge of real-time nonlinear MHE is addressed by adopting an efficient structure-exploiting algorithm within a real-time iteration scheme. In order to facilitate the industrial validation and verification, the algorithm is implemented using an Airbus graphical symbol library to be compliant with the actual flight control computer, and its feasibility of real-time computation has been validated. The simulation results on the RECONFIGURE benchmark, which is a high-fidelity Airbus simulator, over a wide range of the flight envelop show the efficacy of the proposed approach.**

***Index Terms*— Aerospace, fault detection and isolation (FDI), moving horizon estimation (MHE), real-time computation.**

## I. Introduction

DURING aircraft operations, air data measurements are fed into the flight control computer (FCC) to calculate the flight control law, and thus it is critical to ensure availability and reliability of air data measurements [1]. The industrial state-of-the-art for civil aircraft relies on triplex hardware redundancy, and performs a majority voting scheme to select the reliable measurements and discard any failed sources [1]. This scheme works well if only one sensor source becomes faulty, but it is inadequate to address simultaneous multiple sensor faults within the triplex redundancy. As recently investigated in the RECONFIGURE project [1], one possibility to extend guidance and control functionalities without adding additional redundant sensors could be the incorporation of analytical redundancy to: 1) detect and isolate sensor faults and 2) provide reliable air data estimation.

Reliable state/parameter estimation in the presence of faults highly relies on accurate and prompt fault detection and isolation (FDI). The combination of these two tasks is referred to as fault-tolerant estimation (FTE) in some literature, e.g., the multiple-model approach in [2]–[4], the adaptive Kalman filtering approach in [5] and [6], and the moving horizon estimation (MHE) approach exploiting a sparsity constraint on faults in [7]. FTE is also an important part in a fault-tolerant control system [8], [9]. Depending on the type of adopted model, existing FDI and estimation approaches for aircraft sensors can be classified into two categories. The first category uses an aerodynamics-dependent model (see [10]–[15]). The FDI and estimation methods for such a model need to explicitly address the robustness against uncertain aerodynamics. Moreover, the aerodynamic coefficients highly depend on the specific aircraft structure and flight envelop, and thus the corresponding FDI and estimation methods might fail in any unexpected condition [16]. In contrast, the second category adopts an aerodynamics-independent model, e.g., the wind velocity triangle [17]–[19], the aircraft dynamic model with three-axis load factors as inputs [20]–[22], or a combination of the above-mentioned two models [16], [23]. Such aerodynamics-independent models simplify the design of FDI and estimation algorithms by avoiding the use of uncertain aerodynamics; hence, the corresponding algorithms can be easily configured for different aircrafts without adapting to the changing aerodynamics [16], [20].

To achieve air data estimation tolerant to sensor faults, a crucial issue is to distinguish wind disturbances from faults in FDI [24]. With the assumption of constant winds, an extended Kalman filter (EKF) was developed in [17]–[19] to estimate both winds and the airspeed calibration factor by utilizing the wind velocity triangle. The limitation of this approach is that the estimation performance is highly affected by the fulfilment of the persistence of excitation condition that is not satisfied in some aircraft maneuvers [18], [19]. In [20], it was shown that the airspeed-based kinematic model is not affected under constant winds. Moreover, the ground speed-based kinematic model is insensitive to time-varying winds, and it was used in [21] to address the inertial measurement unit sensor fault reconstruction problem by an adaptive two-stage EKF. For an aerodynamics-dependent model subject to winds, the disturbance decoupling method based on differential geometry was adopted in [10] to perfectly decouple the wind effect in the generated residual signal. In [25], another aerodynamic-dependent Takagi–Sugeno fuzzy model was established to represent the nonlinear dynamics without considering the wind

Manuscript received February 1, 2017; revised November 17, 2017; accepted January 27, 2018. Date of publication February 23, 2018; date of current version April 11, 2019. Manuscript received in final form February 6, 2018. This work was supported by the European Union's Seventh Framework Programme (FP7-RECONFIGURE/2007–2013) under Grant 314544. Recommended by Associate Editor B. Jiang. *(Corresponding author: Yiming Wan.)*

Y. Wan is with the School of Automation, Huazhong University of Science and Technology, Wuhan 430074, China, and also with the Massachusetts Institute of Technology, Cambridge, MA 02139 USA (e-mail: ywan@mit.edu).

T. Keviczky is with the Delft Center for Systems and Control, Delft University of Technology, 2628 CD Delft, The Netherlands (e-mail: t.keviczky@tudelft.nl).

Color versions of one or more of the figures in this paper are available online at http://ieeexplore.ieee.org.

Digital Object Identifier 10.1109/TCST.2018.2804332

effect, and a bank of sliding mode observers were designed for sensor fault diagnosis and estimation.

In contrast to the above-mentioned literature that considers either FDI or estimation of one particular air data parameter, this paper focuses on fault-tolerant air data estimation subject to simultaneous angle-of-attack (AOA) and calibrated airspeed (VCAS) sensor faults. This problem involves two main challenges.

1) Wind disturbances and latent sensor faults simultaneously affect VCAS measurements. On the one hand, the wind estimates are necessary in the FTE to reconstruct AOA and VCAS reliably. On the other hand, the wind estimates also compensate for any undetected fault effect, which makes the generated residual signal much less sensitive to the faults.
2) In order to facilitate industrial validation and verification (V&V), the algorithm implementation needs to use an Airbus graphical symbol library called specification assistee par ordinateur (SAO). This library allows automatic code generation for the FCCs used by Airbus, but includes a significantly limited set of mathematical operation blocks [26], [27]. Such a strict constraint limits the complexity level of the implemented algorithm to be compliant with the actual FCCs.

In order to address the above-mentioned challenges, we propose a fault-tolerant estimator by solving a constrained MHE (CMHE) problem in real time. This approach exploits a low-order aerodynamics-independent model augmented with first-order integrating wind dynamics. By exploiting constraints, the proposed MHE-based constrained residual generator has improved sensitivity to faults compared with conventional unconstrained residual generators, if some inequality constraints are activated by the faults. Such fault sensitivity improvement is shown by nonlinear programming sensitivity analysis, and can be achieved by any general MHE-based FDI incorporating constraints. The implementation challenge of our proposed MHE-based FTE method is addressed by adopting a real-time iteration scheme with interior-point (IP) sequential quadratic programming (SQP) strategies. It ensures fixed computational cost per sample by limiting the number of iterations and admitting suboptimal solutions. The real-time feasibility of our algorithm implementation on FCCs has been validated by the industrial V&V.

Compared with our preliminary results in [28] and [29], our presented approach in this paper additionally incorporates the ground speed measurements in order to reliably estimate AOA after the total loss of the three redundant AOA sensors. In contrast to the desktop simulations in [28] and [29], the results of the industrial validation campaign are presented in this paper to illustrate its real-time feasibility and the promising FDI and estimation performance statistics.

This paper is organized as follows. Section II reviews the objectives, the system model, and challenges in the problem under investigation. Our FTE scheme is proposed in Section III. Then, the advantages of the inequality constraints exploited in FTE are explained in Section IV by comparing with an unconstrained MHE (UMHE)-based FTE. Section V discusses the implementation of our proposed method for real-time computation. In Section VI, the FDI and estimation performance of our implemented method is assessed in the high-fidelity nonlinear RECONFIGURE benchmark by intensive simulation runs covering a wide range of the flight envelop.

## II. Problem Formulation

Civil aircraft are generally equipped with three dedicated sensors for each one of AOA and VCAS measurements. The majority voting scheme is then performed among the three redundant sensors to isolate any faulty sensors and compute a consolidated measurement. Such a triplex redundancy-based majority voting scheme works well when only one sensor source is faulty. However, it cannot effectively isolate multiple faulty sources within the triplex redundancy [1]. The objective of this paper is to enhance the available hardware redundancy by FTE, which includes detecting and isolating simultaneous multiple faulty AOA and VCAS sensors, and at the same time, providing reliable estimation of AOA and VCAS. Considering the two main challenges explained in Section I, the proposed FTE method should have fast fault detection, very low rate of false alarms and missed detections, small estimation errors, and allow feasible real-time computational cost for the FCCs.

### A. Aerodynamics-Independent Model Subject to Winds

The RECONFIGURE project focuses on the longitudinal motion of the aircraft. Thus, the following longitudinal model is derived for FTE of AOA and VCAS:

$$\begin{cases} \dot{\alpha}(t) = \mathscr{F}_{\alpha}\left(\alpha(t), \Theta(t)\right) + u_{\alpha}(t) \\ \dot{V}_g(t) = \mathscr{F}_{v}\left(\alpha(t), \Theta(t)\right) + u_{v}(t) \\ \dot{\mathbf{w}}(t) = \mathbf{u}_{w}(t) \\ \mathbf{y}(t) = h\left(\alpha(t), \mathbf{w}(t), \Theta(t)\right) \\ \mathbf{y}_m(t) = \mathbf{y}(t) + \mathbf{n}(t) \end{cases} \tag{1}$$

with the definitions $\mathbf{w}(t) = [W_x(t)\ W_z(t)]^T$, $\mathbf{u}_w(t) = [u_{w,x}(t)\ u_{w,z}(t)]^T$, $\mathbf{y}(t) = [V_g(t)\ V_z(t)\ \alpha(t)\ V_c(t)]^T$

$$\Theta(t) = [V_g(t) \quad \theta(t) \quad q(t) \quad A_x(t) \quad A_z(t) \quad z(t)]^T \tag{2}$$

and $\mathbf{n}(t) = [n_{vg}(t)\ n_{vz}(t)\ n_{\alpha}(t)\ n_{vc}(t)]^T$. The system outputs $\mathbf{y}(t)$ include the ground speed $V_g$, the vertical speed $V_z$, the AOA $\alpha$, and the VCAS $V_c$. $W_x$ and $W_z$ represent the horizontal and vertical wind speeds in the inertial frame, respectively. The model parameter $\Theta$ consists of ground speed $V_g$, pitch angle $\theta$, pitch rate $q$, horizontal load factor $A_x$, vertical load factor $A_z$, and altitude $z$, which are all measurable. The reason of including $V_g$, which is one entry of the system outputs, in the model parameter $\Theta$ will be explained later in Remark 1. The output equations in (1) for $V_z$ and $V_c$ are

$$V_z = h_{vz}(\alpha, \mathbf{w}, \Theta) \quad \text{and} \quad V_c = h_{vc}(\alpha, \mathbf{w}, \Theta) \tag{3}$$

respectively. The unknown inputs $u_{\alpha}$, $u_v$, and $\mathbf{n}$ account for the effects of process noises, measurement noises, and the model mismatches. For each redundant AOA sensor measurement $\alpha_m^{(i)}$ or VCAS sensor measurement $V_{c,m}^{(i)}$, $i = 1, 2, 3$, the latent sensor faults $f_{\alpha}^{(i)}$ and $f_{vc}^{(i)}$ are additive, that is

$$\alpha_m^{(i)} = \alpha + f_{\alpha}^{(i)} + n_{\alpha}^{(i)}, \quad V_{c,m}^{(i)} = V_c + f_{vc}^{(i)} + n_{vc}^{(i)}. \tag{4}$$

The first-order integrating model in (1) is a simple yet powerful approximation of the wind dynamics that has been widely used in flight control in [30]. $u_{w,x}$ and $u_{w,z}$ represent the unknown horizontal and vertical wind accelerations.

The above-mentioned system model (1) provides several advantages: 1) it avoids using other air data measurements which are considered as unreliable in the presence of AOA or VCAS sensor faults, and involves only inertial sensors associated with the model parameter $\Theta$ and the output $\mathbf{y}_m$; 2) it includes no aerodynamic parameters, and thus it is independent of aircraft and flight envelop; 3) it is insensitive to actuator faults and structural damages; and 4) its low state dimensions are attractive for real-time computation.

More details of the aerodynamics-independent longitudinal model (1) are explained in the following. Let $\begin{bmatrix} u & v & w \end{bmatrix}^\top$ denote the components of the true airspeed $V_t$ in the body frame, whose relation to $V_t$ is expressed as follows with the AOA $\alpha$ and the sideslip angle $\beta$:

$$\begin{bmatrix} u \\ v \\ w \end{bmatrix} = \begin{bmatrix} V_t \cos\alpha \cos\beta \\ V_t \sin\beta \\ V_t \sin\alpha \cos\beta \end{bmatrix}.$$

The load factors $A_x, A_y$, and $A_z$ represent the accelerations generated by the aerodynamic forces along the axes of the body frame. The wind speed components in the inertial frame are denoted by $[W_x \ W_y \ W_z]^\top$. The roll, pitch, and yaw angles are given by $[\phi \ \theta \ \psi]^T$, respectively, while the roll, pitch, and yaw rates are $[p \ q \ r]^T$ accordingly.

With the above-mentioned notations, the aircraft dynamics is expressed by [31]

$$\begin{bmatrix} \dot{u} \\ \dot{v} \\ \dot{w} \end{bmatrix} = \begin{bmatrix} A_x \\ A_y \\ A_z \end{bmatrix} + R_{\mathrm{BI}} \begin{bmatrix} 0 \\ 0 \\ g \end{bmatrix} - \begin{bmatrix} p \\ q \\ r \end{bmatrix} \times \begin{bmatrix} u \\ v \\ w \end{bmatrix} - R_{\mathrm{BI}} \begin{bmatrix} \dot{W}_x \\ \dot{W}_y \\ \dot{W}_z \end{bmatrix} \tag{5}$$

where $g$ denotes the gravitational acceleration, and $R_{\mathrm{BI}}$ represents the rotational matrix governed by $[\phi \ \theta \ \psi]^T$ to transform a vector in the inertial frame to a vector in the body frame. Since the RECONFIGURE project focuses on the longitudinal motion by assuming negligible lateral motion and constant wind component $W_y$, we have $v = 0$, $\beta = 0$, $A_y = 0$, $\dot{W}_y = 0$, $\phi = 0$, $\psi = 0$, $p = 0$, and $r = 0$. This results in the simplified longitudinal dynamics

$$\begin{bmatrix} \dot{u} \\ \dot{w} \end{bmatrix} = \begin{bmatrix} A_x \\ A_z \end{bmatrix} + R_{\mathrm{BI}} \begin{bmatrix} 0 \\ g \end{bmatrix} + \begin{bmatrix} -qw \\ qu \end{bmatrix} - R_{\mathrm{BI}} \begin{bmatrix} \dot{W}_x \\ \dot{W}_z \end{bmatrix} \tag{6}$$

derived from (5), with

$$\begin{bmatrix} u \\ w \end{bmatrix} = \begin{bmatrix} V_t \cos\alpha \\ V_t \sin\alpha \end{bmatrix}, \quad R_{\mathrm{BI}} = \begin{bmatrix} \cos\theta & -\sin\theta \\ \sin\theta & \cos\theta \end{bmatrix}. \tag{7}$$

Note that using the measured load factors $A_x$ and $A_z$, the dynamic relation (6) becomes independent of aerodynamics, and thus it is valid for different aircrafts with different flight envelops. Instead of directly using (6) for our problem, we choose to work with the following equivalent model derived from (6) by exploiting (7):

$$\dot{\alpha} = \frac{1}{V_t} f_\alpha(\alpha, \Theta) + q + \frac{1}{V_t} f_{w,\alpha}(\alpha, \mathbf{w}, \Theta) \tag{8}$$

$$\dot{V}_t = f_v(\alpha, \Theta) - f_{w,v}(\alpha, \mathbf{w}, \Theta) \tag{9}$$

with

$$\begin{aligned} f_\alpha(\alpha, \Theta) &= -A_x \sin\alpha + A_z \cos\alpha + g\cos(\alpha - \theta) \\ f_{w,\alpha}(\alpha, \mathbf{w}, \Theta) &= \dot{W}_x \sin(\alpha - \theta) - \dot{W}_z \cos(\alpha - \theta) \\ f_v(\alpha, \Theta) &= A_x \cos\alpha + A_z \sin\alpha + g\sin(\alpha - \theta) \\ f_{w,v}(\alpha, \mathbf{w}, \Theta) &= \dot{W}_x \cos(\alpha - \theta) + \dot{W}_z \sin(\alpha - \theta). \end{aligned}$$

Note that measurements of the true airspeed $V_t$ are unreliable in the presence of VCAS sensor fault [1], and thus should not be directly used for the VCAS sensor fault diagnosis. In this case, we replace $V_t$ in (8) with the function

$$\begin{aligned} V_t = h_{vt}(\alpha, \mathbf{w}, \Theta) &= -W_x \cos(\alpha - \theta) - W_z \sin(\alpha - \theta) \\ &\quad + \sqrt{V_g^2 - [W_x \sin(\alpha - \theta) - W_z \cos(\alpha - \theta)]^2} \end{aligned} \tag{10}$$

which can be derived from the wind velocity triangle [17, eq. (1)], [32, eq. (1.5-6)]

$$\begin{cases} V_g^2 = u_g^2 + w_g^2 \\ u_g = u + W_x \cos\theta - W_z \sin\theta \\ w_g = w + W_x \sin\theta + W_z \cos\theta. \end{cases}$$

In order to derive a simplified yet reliable model without involving $V_t$, we make the following approximations. For the civil aircraft in the RECONFIGURE project [1], we have $V_g \gg |W_x \sin(\alpha - \theta) - W_z \cos(\alpha - \theta)|$, and then (10) can be approximated as

$$h_{vt}(\alpha, \mathbf{w}, \Theta) \approx -W_x \cos(\alpha - \theta) - W_z \sin(\alpha - \theta) + V_g. \tag{11}$$

Let $\Delta V = V_t - V_g$ denote the difference between the true airspeed $V_t$ and the ground speed $V_g$ due to the winds. Since we have

$$V_g^2 \gg \Delta V \ f_\alpha(\alpha, \Theta), \quad V_t \gg f_{w,\alpha}(\alpha, \mathbf{w}, \Theta)$$

for the considered flight scenarios, the approximations

$$\frac{1}{V_t} f_\alpha(\alpha, \Theta) \approx \left( \frac{1}{V_g} - \frac{1}{V_g^2} \Delta V \right) f_\alpha(\alpha, \Theta) \approx \frac{1}{V_g} f_\alpha(\alpha, \Theta)$$

$$\frac{1}{V_t} f_w(\alpha, \mathbf{w}, \Theta) \approx 0$$

can be used to derive

$$\dot{\alpha} = \frac{1}{V_g} f_\alpha(\alpha, \Theta) + q + u_\alpha \tag{13}$$

from (8). Similarly, by exploiting (8), (11), and $\dot{\theta} = q$, we are able to approximate (9) with

$$\dot{V}_g = f_v(\alpha, \Theta) + u_v. \tag{14}$$

Equations (13) and (14) represent the first two equations of the model (1), and $u_\alpha$ and $u_v$ account for the model mismatches including the above-mentioned unknown approximation errors and the effect of stochastic noises in the measured parameters $\Theta$.

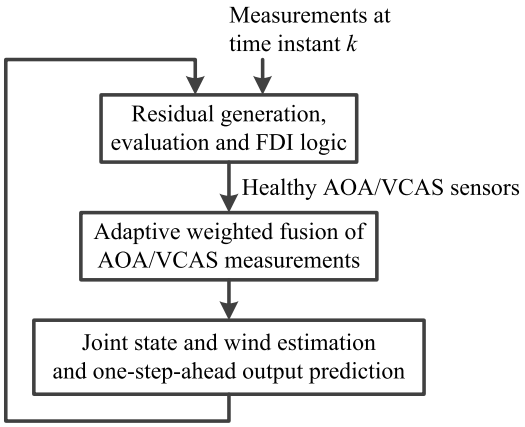


Fig. 1. FTE scheme.

With the airspeed $V_t$ in the body frame and the vertical wind $W_z$ in the inertial frame, the vertical speed measurement $V_{z,m}$ in the inertial frame is expressed by [32, eq. (2.4-5)]

$$V_{z,m} = -V_t \sin(\alpha - \theta) + W_z + n_{vz}$$

which can be further approximated as

$$V_{z,m} = -V_g \sin(\alpha - \theta) + W_z + n_{vz} \tag{15}$$

due to (11) and $\alpha - \theta \approx 0$.

The output equation for the fault-free VCAS measurement $V_{c,m}$ consists of two conversions: 1) from ground speed $V_g$ to true airspeed $V_t$ via the function $h_{vt}(\alpha, \mathbf{w}, \Theta)$ in (10) and (11) and 2) from $V_t$ to $V_c$ [33], [34], that is

$$\begin{aligned} V_{c,m} &= \sqrt{5\gamma\, RT_0}\varrho(V_t, T, \bar{p}) + n_{vc}, \\ &= \sqrt{5\gamma\, RT_0}\varrho\left(h_{vt}(\alpha, \mathbf{w}, \Theta), T, \bar{p}\right) + n_{vc} \end{aligned} \tag{16}$$

with $T = T_0 + Lz$, $\bar{p} = (1 + (L/T_0)z)^{(g/-RL)}$

$$\varrho(V_t, T, \bar{p}) = \sqrt{\left[\left(\left(1 + \frac{V_t^2}{5\gamma\, RT}\right)^{3.5} - 1\right)\bar{p} + 1\right]^{\frac{1}{3.5}} - 1}$$

where $z$, $T$, and $\bar{p}$ represent the pressure altitude, the outside air temperature, and the static pressure scaled by the ground static pressure value, respectively. The constants $T_0$, $L$, $R$, and $\gamma$ take their values according to International Standard Atmosphere [33]: $T_0 = 288.15\,\text{K}$, $L = -6.5\,\text{K/km}$, $R = 287.05287\,(\text{m/s})^2\,\text{K}$, and $\gamma = 1.4$. $z$ in $\Theta$, $T$, and $\bar{p}$ in (16) uses altitude measurements. $n_{vz}$ and $n_{vc}$ account for both the unknown approximation errors and the stochastic measurement noises in (15) and (16), respectively.

## III. Fault-Tolerant Moving Horizon Estimation Scheme

### A. Fault-Tolerant Estimation Scheme

As depicted in Fig. 1, our proposed FDI and estimation scheme consists of three consecutive steps.

*Step 1 (Residual Generation, Evaluation, and FDI Logic):* The residual signals for FDI are generated as the difference between the AOA/VCAS measurements $\{\alpha_{m,k}^{(i)}, V_{c,m,k}^{(i)}\}$ and their one-step-ahead predictions $\{\hat{\alpha}_{k|k-1}, \hat{V}_{c,k|k-1}\}$, that is

$$r_{\alpha,k}^{(i)} = \alpha_{m,k}^{(i)} - \hat{\alpha}_{k|k-1}, \quad r_{vc,k}^{(i)} = V_{c,m,k}^{(i)} - \hat{V}_{c,k|k-1} \tag{17}$$

for $i = 1, 2, 3$. Here, the index $k$ denotes the samples at time instant $t_k$. The residual signals are evaluated by their root-mean-square (rms) values over a sliding window

$$J_{\star,k}^{(i)} = \sqrt{\frac{1}{N_{\text{eval}}} \sum_{j=k-N_{\text{eval}}+1}^{k} \left(r_{\star,j}^{(i)}\right)^2} \tag{18}$$

where $\star$ represents "$\alpha$" and "$vc$," and $N_{\text{eval}}$ is the length of residual evaluation window. With a suitable threshold $J_{\star,\text{th}}$, the $i$th AOA or VCAS sensor is concluded to be faulty if we have $J_{\star,k}^{(i)} > J_{\star,\text{th}}$ for $n_D$ times during the past time window $[k - N_{\text{eval}} + 1, k]$, which allows a confirmation time for the fault detection decision.

*Step 2 (Adaptive Weighted Fusion of AOA/VCAS Measurements):* Similar to [20], the redundant AOA sensors identified as fault-free are fused into a weighted mean measurement $\alpha_m$

$$\begin{aligned} \alpha_{m,k} &= \sum_{i \in \left\{J_{\alpha,k}^{(i)} \le J_{\alpha,\text{th}}\right\}} \beta_{\alpha,k}^{(i)} \alpha_{m,k}^{(i)} \\ \beta_{\alpha,k}^{(i)} &= \frac{1}{\sum_{j \in \left\{J_{\alpha,k}^{(j)} \le J_{\alpha,\text{th}}\right\}} \frac{1}{\left(J_{\alpha,k}^{(j)}\right)^2}} \frac{1}{\left(J_{\alpha,k}^{(i)}\right)^2}. \end{aligned} \tag{19}$$

The above-mentioned weights $\beta_{\alpha,k}^{(i)}$ are adaptively computed from the residual rms values (18), so that the sensors with larger residual rms values are assigned with lower weights. The same procedure is performed on the VCAS sensors to compute the weights $\beta_{vc,k}^{(i)}$ and the weighted mean value $V_{c,m,k}$. Before a faulty sensor is detected, the undetected faulty sensor is given a lower weight in (19) due to its larger residual rms value. These adaptively fused measurements are used in the subsequent state and wind estimation; thus, the state and wind estimates are less affected by the undetected faults embedded in the lower weighted sensors.

*Step 3 (Joint State and Wind Estimation and One-Step-Ahead Output Prediction):* The joint state and wind estimation algorithm computes the filtered estimates $\hat{\alpha}_{k-1|k-1}$ and $\hat{\mathbf{w}}_{k-1|k-1}$ by solving a nonlinear MHE problem that incorporates the bounds of the states and the noisy inputs of the model (1). It then generates the one-step-ahead predictions $\hat{\alpha}_{k|k-1}$ and $\hat{V}_{c,k|k-1}$ for the residual generation and evaluation in Step 1 mentioned before.

As will be explained in Section IV, the incorporated constraints in Step 3 effectively improve the fault sensitivity of the generated residual signals.

### B. Overview of Moving Horizon Estimation

The MHE technique is well known for its capability to address nonlinearity, constraints, and robustness to initial errors [35]. It builds on the discrete-time approximation of

the continuous-time model (1)

$$\alpha_{k+1} = \alpha_k + t_s \mathscr{F}_\alpha(\alpha_k, \Theta_k) + t_s u_{\alpha,k} \tag{20a}$$
$$V_{g,k+1} = V_{g,k} + t_s \mathscr{F}_v(\alpha_k, \Theta_k) + t_s u_{v,k} \tag{20b}$$
$$\mathbf{w}_{k+1} = \mathbf{w}_k + t_s \mathbf{u}_{w,k} \tag{20c}$$
$$\bar{\mathbf{y}}_{m,k} = h(\alpha_k, \mathbf{w}_k, \Theta_k) + \bar{\mathbf{n}}_k \tag{20d}$$

where $t_s$ is the sampling interval and (20a)–(20c) are obtained via approximated numerical integration applied to (1). In (20d), the output vector $\bar{\mathbf{y}}_{m,k}$ consists of the ground speed measurement $V_{g,m}$, the vertical speed measurement $V_{z,m}$, and the two fused measurements $\alpha_m$ and $V_{c,m}$ defined in (19). Accordingly, $\bar{\mathbf{n}}_k = [n_{vg,k}\ n_{vz,k}\ n_{\alpha,k}\ n_{vc,k}]^T$ includes the measurement noises, where $n_{\alpha,k}$ and $n_{vc,k}$ are the fused noises

$$n_{\star,k} = \sum_{i \in \left\{ J^{(i)}_{\star,k} \le J_{\star,\text{th}} \right\}} \beta^{(i)}_{\star,k} n^{(i)}_{\star,k},\ \star \text{ represents } \alpha \text{ or } vc$$

for the fused measurements $\alpha_m$ and $V_{c,m}$ defined in (19). Note that the fault diagnosis decision determines whether or not to include the AOA and VCAS measurements in the output vector $\bar{\mathbf{y}}_{m,k}$. With different configurations of the output vector, the observability property changes, as will be explained in Section III-C.

Given a moving horizon consisting of $N$ samples of output measurements $\{\bar{\mathbf{y}}_{m,l}, \bar{\mathbf{y}}_{m,l+1}, \ldots, \bar{\mathbf{y}}_{m,k}\}$ $(l = k - N + 1)$ at time instant $k$, the MHE problem is formulated as

$$\min_{\mathbf{x}_i, \mathbf{u}_i} \ \frac{1}{2} \left\| \mathbf{x}_l - \mathbf{x}^-_{l|k} \right\|^2_{\mathbf{P}^{-1}} + \frac{1}{2} \sum_{i=l}^{k-1} \|\mathbf{u}_i\|^2_{\mathbf{Q}^{-1}} \tag{21a}$$
$$+ \frac{1}{2} \sum_{i=l}^{k} \|\bar{\mathbf{y}}_{m,i} - h(\mathbf{x}_i, \Theta_i)\|^2_{\mathbf{R}^{-1}}$$
$$\text{s.t. } \mathbf{x}_{i+1} = F(\mathbf{x}_i, \mathbf{u}_i, \Theta_i),$$
$$\mathbf{u}^{\text{LB}}_i \le \mathbf{u}_i \le \mathbf{u}^{\text{UB}}_i, \quad i = l, \ldots, k-1$$
$$\mathbf{x}^{\text{LB}}_i \le \mathbf{x}_i \le \mathbf{x}^{\text{UB}}_i, \quad i = l, \ldots, k \tag{21b}$$

where $\|\mathbf{s}\|^2_{\mathbf{M}^{-1}}$ in (21a) for a vector $\mathbf{s}$ and a positive definite matrix $\mathbf{M}$ represents a weighted vector norm computed as $\mathbf{s}^T\mathbf{M}^{-1}\mathbf{s}$

$$\mathbf{x} = \begin{bmatrix} \alpha \\ V_g \\ \mathbf{w} \end{bmatrix}, \quad \mathbf{u} = \begin{bmatrix} u_\alpha \\ u_v \\ \mathbf{u}_w \end{bmatrix}, \ \mathbf{P} = \text{diag}(p_\alpha, p_v, p_w \mathbf{I}_2)$$
$$\mathbf{Q} = \text{diag}(q_\alpha, q_v, q_w \mathbf{I}_2), \quad \mathbf{R} = \text{diag}(R_\alpha, R_{vz}, R_{vc}). \tag{22}$$

The function $F(\cdot)$ in (21b) represents the right-hand sides of (20a)–(20c), and $h(\mathbf{x}_i, \Theta_i)$ is a compact form of $h(\alpha_i, \mathbf{w}_i, \Theta_i)$ defined in (20d). The bounds of the inequality constraints in (21b) can be time varying to account for different weather or flight conditions. At each time instant $k$, given the initial condition $\mathbf{x}^-_{l|k}$ and the output sequence $\{\bar{\mathbf{y}}_{m,i}, l \le i \le k\}$, the nonlinear programming problem (21) is solved to compute the sequence of state estimates $\hat{\mathbf{x}}_{l|k}, \ldots, \hat{\mathbf{x}}_{k|k}$, where the filtered estimate $\hat{\mathbf{x}}_{k|k}$ is used to compute the one-step-ahead AOA and wind predictions. The first term of the objective function (21a) is the so-called arrival cost to account for data before the current estimation horizon. Here, we do not adopt a statistical interpretation of the arrival cost as in [36], which requires heavy computations to update $\mathbf{x}^-_{l|k}$ and $\mathbf{P}$ to represent the information given by the filtered or smoothed density function of $\mathbf{x}_l$. Instead, similar to [37], the arrival cost term is updated in a deterministic sense in this paper: we assign $\mathbf{x}^-_{l|k}$ to be the *a priori* smoothed state estimate $\hat{\mathbf{x}}_{l|k-1}$ obtained by solving (21) over the previous horizon $[l-1, k-1]$, and use $\mathbf{P}$, $\mathbf{Q}$, and $\mathbf{R}$ as tuning parameters to achieve tradeoffs between different components of the objective function.

TABLE I
FOUR CATEGORIES OF FAULT SCENARIOS AND CONFIGURATIONS OF OUTPUTS USED IN THE MHE

| Fault category | Number of faulty AOA and VCAS sensors | Configuration of $\bar{\mathbf{y}}_m$ in (20d) |
|---|---|---|
| I | $N^f_\alpha < 3, N^f_v < 3$ | $[V_{g,m} \quad V_{z,m} \quad \alpha_m \quad V_{c,m}]^{\text{T}}$ |
| II | $N^f_\alpha = 3, N^f_v < 3$ | $[V_{g,m} \quad V_{z,m} \quad V_{c,m}]^{\text{T}}$ |
| III | $N^f_\alpha < 3, N^f_v = 3$ | $[V_{g,m} \quad V_{z,m} \quad \alpha_m]^{\text{T}}$ |
| IV | $N^f_\alpha = 3, N^f_v = 3$ | $[V_{g,m} \quad V_{z,m}]^{\text{T}}$ |

Throughout this paper, the MHE problem (21) with or without inequality constraints is referred to as CMHE or UMHE, respectively. The benefit of incorporating constraints in residual generation will be analyzed in Section IV by comparing CMHE with UMHE in terms of fault sensitivity. The real-time CMHE implementation will be discussed in Section V.

### C. Observability Analysis

Let $N^f_\alpha$ and $N^f_v$ represent the number of faulty AOA and VCAS sensors, respectively. As illustrated in Table I, there are four different categories of faulty scenarios, and the output $\bar{\mathbf{y}}_m$ in (20d) needs to be configured accordingly after removing the identified faulty AOA and VCAS sensors.

Although the proposed method can detect and isolate arbitrary number of AOA and VCAS sensor faults, the reliability of the AOA and VCAS estimates after removing faulty sensors is related to the local observability of the nonlinear discrete-time system (20) under different configurations of $\bar{\mathbf{y}}_m$. For the configuration I in Table I, the matrices of the linearized model ($\mathbf{A}_k, \mathbf{B}_k$, and $\mathbf{C}_k$) of the discrete-time system (20) have the structure

$$\mathbf{A}_k = \begin{bmatrix} a_{11,k} & a_{12,k} & 0 & 0 \\ a_{21,k} & 1 & 0 & 0 \\ 0 & 0 & 1 & 0 \\ 0 & 0 & 0 & 1 \end{bmatrix}$$
$$\mathbf{C}_k = \begin{bmatrix} 0 & 1 & 0 & 0 \\ c_{21,k} & c_{22,k} & 0 & 1 \\ 1 & 0 & 0 & 0 \\ c_{41,k} & 0 & c_{43,k} & c_{44,k} \end{bmatrix} \tag{23}$$

with the state vector defined in (22).

*Remark 1:* It is worth noting that the ground speed measurements $V_{g,m}$ are included in the output vector $\bar{\mathbf{y}}_m$ to improve observability of the state $\alpha$ after removing the AOA measurements in configurations II and III. It is not of primary concern to estimate the state $V_g$ in our problem since we

have its fault-free measurement $V_{g,m}$. Because of this reason, we regard $V_g$ as a time-varying measured parameter rather than an unknown state in (11), (15), (16), and (20a), which explains why $V_g$ is included in the model parameter $\Theta$ in (2). Therefore, we actually have $a_{12,k} = c_{22,k} = 0$ in (23), which simplifies matrix manipulations in the algorithm implementation explained in Section V-C.

Based on the above-mentioned linearized model (23), we can make the following observations.

1) The states $\alpha$, $V_g$, and $W_z$ are locally observable in all the above-mentioned four configurations of $\bar{\mathbf{y}}_m$ thanks to the availability of the ground speed $V_{g,m}$ and the vertical speed $V_{z,m}$ measurements.
2) Due to different numerical ranges of physical variables, the local observability during certain aircraft maneuvers may become weak, which can possibly cause numerical problems in the nonlinear programming-based CMHE algorithm. This is especially the case in configurations II and IV where the AOA is to be estimated after losing AOA measurements. This issue can be alleviated by selecting suitable weighting matrices, in order to improve the numerical conditioning of the QP subproblems in Section V-A.
3) The observability of the horizontal wind $W_x$ is attributed only to the availability of VCAS measurements. When we have no VCAS measurements as in configurations III and IV, $W_x$ becomes neither observable nor detectable (the unobservable $W_x$ cannot be asymptotically reconstructed; see the definition of $N$-detectability in [38]), and consequently VCAS cannot be reconstructed.

## IV. Fault Sensitivity of MHE-Based Residual

In this section, we will analyze the improvement of fault sensitivity by exploiting the inequality constraints in the CMHE-based FTE (CMHE-FTE). This is done via nonlinear sensitivity analysis to compare the CMHE-FTE with the UMHE-based FTE (UMHE-FTE).

Before a rigorous analysis, some intuitive explanations are first given as follows. Sensor faults contaminate the measurements before being detected. In the UMHE-FTE, the state and wind estimates compensate for the fault effect when minimizing the objective function (21a), and thus the output residuals (17) might be still small even in the presence of faults. In contrast, the CMHE-FTE respects the inequality constraints in (21b). When the presence of faults causes some inequality constraints to become active, the state and wind estimates would be restricted by the active constraints and reluctant to compensate for the fault effect; thus, the residuals become more sensitive to faults.

### A. Fault Sensitivity of Unconstrained-MHE-Based Residual

Let $\mathbf{f}_k$ denote the sensor fault vector included in the measurement $\bar{\mathbf{y}}_{m,k}$. By defining

$$\mathbf{z}_k = \begin{bmatrix}\mathbf{x}_l^T & \mathbf{u}_l^T & \cdots & \mathbf{x}_{k-1}^T & \mathbf{u}_{k-1}^T & \mathbf{x}_k^T\end{bmatrix}^T \tag{24}$$

$$\mathcal{I}_k = \begin{bmatrix}(\mathbf{x}_{l|k}^-)^T & \mathbf{0}^T & \bar{\mathbf{y}}_{m,l}^T & \cdots & \mathbf{0}^T & \bar{\mathbf{y}}_{m,k-1}^T & \bar{\mathbf{y}}_{m,k}^T\end{bmatrix}^T \tag{25}$$

$$\epsilon_k = \begin{bmatrix}\mathbf{0}^T & \mathbf{0}^T & \mathbf{f}_l^T & \cdots & \mathbf{0}^T & \mathbf{f}_{k-1}^T & \mathbf{f}_k^T\end{bmatrix}^T \tag{26}$$

$$\mathbf{V} = \operatorname{diag}(\mathbf{P}, \mathbf{Q}, \mathbf{R}, \ldots, \mathbf{Q}, \mathbf{R}, \mathbf{R})$$

$$F_1(\mathbf{z}_k) = \begin{bmatrix}\mathbf{x}_l^T & \mathbf{u}_l^T & h^T(\mathbf{x}_l, \Theta_l) & \cdots \\ & \mathbf{u}_{k-1}^T & h^T(\mathbf{x}_{k-1}, \Theta_{k-1}) & h^T(\mathbf{x}_k, \Theta_k)\end{bmatrix}^T$$

$$F_2(\mathbf{z}_k) = \begin{bmatrix}\mathbf{x}_{l+1} - F(\mathbf{x}_l, \mathbf{u}_l, \Theta_l) \\ \vdots \\ \mathbf{x}_k - F(\mathbf{x}_{k-1}, \mathbf{u}_{k-1}, \Theta_{k-1})\end{bmatrix}$$

the MHE problem (21) can be compactly written as

$$\hat{\mathbf{z}}_k(\mathcal{I}_k) = \arg\min_{\mathbf{z}_k} \ \frac{1}{2}\|\mathcal{I}_k - F_1(\mathbf{z}_k)\|_{\mathbf{V}^{-1}}^2 \quad \text{s.t. } F_2(\mathbf{z}_k) = \mathbf{0} \tag{27}$$

or equivalently

$$\hat{\mathbf{z}}_k(\mathcal{I}_k^0, \epsilon_k) = \arg\min_{\mathbf{z}_k} \ \frac{1}{2}\left\|\mathcal{I}_k^0 + \epsilon_k - F_1(\mathbf{z}_k)\right\|_{\mathbf{V}^{-1}}^2 \quad \text{s.t. } F_2(\mathbf{z}_k) = \mathbf{0} \tag{28}$$

where the information vector $\mathcal{I}_k$ is decomposed into the nominal part $\mathcal{I}_k^0$ and the fault perturbation $\epsilon_k$, i.e., $\mathcal{I}_k = \mathcal{I}_k^0 + \epsilon_k$. The inequality constraints in (21b) are omitted in this section, and will be discussed in Section IV-B. It can be seen from (27) that the estimate $\hat{\mathbf{z}}_k$ is a function of the information vector $\mathcal{I}_k$. According to (28), the filtered state estimate can be expressed by $\hat{\mathbf{x}}_{k|k} = \mathbf{P}_s\hat{\mathbf{z}}_k(\mathcal{I}_k^0, \epsilon_k)$, with $\mathbf{P}_s = \begin{bmatrix}\mathbf{0} \cdots \mathbf{0} \ \mathbf{I}\end{bmatrix}$. Then, since $\hat{\mathbf{u}}_{k|k} = \mathbf{0}$ is the optimal estimate of $\mathbf{u}_k$ for the MHE problem (21), we construct the one-step-ahead state prediction $\hat{\mathbf{x}}_{k+1|k} = F(\hat{\mathbf{x}}_{k|k}, \hat{\mathbf{u}}_{k|k}, \Theta_k) = F(\hat{\mathbf{x}}_{k|k}, \mathbf{0}, \Theta_k)$ according to (21b), and generate the residual signal as

$$\begin{aligned}\mathbf{r}_{k+1}&\left(\mathcal{I}_{k+1}^0, \epsilon_k, \mathbf{f}_{k+1}\right) \\ &= \bar{\mathbf{y}}_{m,k+1} - \hat{\mathbf{y}}_{k+1|k} \\ &= \bar{\mathbf{y}}_{m,k+1} - h(\hat{\mathbf{x}}_{k+1|k}, \Theta_{k+1}) \\ &= h(\alpha_{k+1}, \mathbf{w}_{k+1}, \Theta_{k+1}) + \mathbf{f}_{k+1} + \bar{\mathbf{n}}_{k+1} \\ &\quad - h\left(F\left(\mathbf{P}_s\hat{\mathbf{z}}_k\left(\mathcal{I}_k^0, \epsilon_k\right), \mathbf{0}, \Theta_k\right), \Theta_{k+1}\right)\end{aligned} \tag{29}$$

according to the output equation (20d). The sensitivity of the residual signal to faults is characterized by the first-order derivative $(\partial\mathbf{r}_{k+1}/\partial(\epsilon_k, \mathbf{f}_{k+1}))$.

*Remark 2:* To analyze disturbance robustness, the output equation (20d) is written into

$$\bar{\mathbf{y}}_{m,k} = h(\alpha_k, \mathbf{0}, \Theta_k) + \mathbf{d}_k + \bar{\mathbf{n}}_k$$

in the fault-free case, with $\mathbf{d}_k = h(\alpha_k, \mathbf{w}_k, \Theta_k) - h(\alpha_k, \mathbf{0}, \Theta_k)$. Then $\epsilon_k$ in (26) is redefined as

$$\epsilon_k = \begin{bmatrix}\mathbf{0}^T & \mathbf{0}^T & \mathbf{d}_l^T & \cdots \mathbf{0}^T & \mathbf{d}_{k-1}^T & \mathbf{d}_k^T\end{bmatrix}^T$$

to represent the disturbance perturbation in (28) in the fault-free case. By replacing $\mathbf{f}_{k+1}$ in (29) with $\mathbf{d}_{k+1}$, we obtain the fault-free residual signal $\mathbf{r}_{k+1}(\mathcal{I}_{k+1}^0, \epsilon_k, \mathbf{d}_{k+1})$. Similar to fault sensitivity, the disturbance robustness of the residual signal in (29) is determined by

$$\frac{\partial\mathbf{r}_{k+1}}{\partial(\epsilon_k, \mathbf{d}_{k+1})}\frac{\partial(\epsilon_k, \mathbf{d}_{k+1})}{\partial(\mathbf{w}_l, \ldots, \mathbf{w}_{k+1})}.$$

Since $(\partial\mathbf{r}_{k+1}/\partial(\epsilon_k, \mathbf{f}_{k+1}))$ in the faulty case is equal to $(\partial\mathbf{r}_{k+1}/\partial(\epsilon_k, \mathbf{d}_{k+1}))$ in the fault-free case, higher fault sensitivity generally implies higher sensitivity to disturbances, i.e., lower disturbance robustness.

In order to derive the fault sensitivity of the residual signal in (29), we first derive the fault sensitivity of the estimate $\hat{\mathbf{z}}_k(\mathcal{I}_k^0, \epsilon_k)$, i.e., $(\partial \hat{\mathbf{z}}_k(\mathcal{I}_k^0, \epsilon_k)/\partial \epsilon_k)$, via sensitivity analysis of the MHE problem (28) parameterized in the fault vector $\epsilon_k$. The Karush–Kuhn–Tucker (KKT) conditions for the optimization problem (28) are given by

$$\mathcal{K}\big(\mathbf{z}_k, \lambda, \mathcal{I}_k^0, \epsilon_k\big) = \begin{bmatrix} -\mathbf{J}_1^T(\mathbf{z}_k)\mathbf{V}^{-1}\big[\mathcal{I}_k^0 + \epsilon_k - F_1(\mathbf{z}_k)\big] + \mathbf{J}_2^T(\mathbf{z}_k)\lambda \\ F_2(\mathbf{z}_k) \end{bmatrix} = \mathbf{0} \tag{30}$$

where we define $\mathbf{J}_1(\mathbf{z}_k) = (\partial F_1(\mathbf{z}_k)/\partial \mathbf{z}_k)$ and $\mathbf{J}_2(\mathbf{z}_k) = (\partial F_2(\mathbf{z}_k)/\partial \mathbf{z}_k)$. The solution to the KKT condition (30) is denoted by $\mathbf{z}_k(\mathcal{I}_k^0, \epsilon_k)$ and $\lambda(\mathcal{I}_k^0, \epsilon_k)$, which are implicit functions of $\mathcal{I}_k^0$ and $\epsilon_k$. The optimal solution associated with the MHE problem (28) is $\hat{\mathbf{z}}_k(\mathcal{I}_k^0, \epsilon_k)$ and $\hat{\lambda}(\mathcal{I}_k^0, \epsilon_k)$. In the neighborhood of the fault vector $\epsilon_k$, we apply the implicit function theorem to yield

$$\frac{\partial \mathcal{K}\big(\mathbf{z}_k, \lambda, \mathcal{I}_k^0, \epsilon_k\big)}{\partial(\mathbf{z}_k, \lambda)} \begin{bmatrix} \dfrac{\partial \hat{\mathbf{z}}_k}{\partial \epsilon_k} \\ \dfrac{\partial \hat{\lambda}}{\partial \epsilon_k} \end{bmatrix} + \frac{\partial \mathcal{K}\big(\mathbf{z}_k, \lambda, \mathcal{I}_k^0, \epsilon_k\big)}{\partial \epsilon_k} = \mathbf{0}$$

which can be rewritten as

$$\begin{bmatrix} \mathbf{H} & \mathbf{J}_2^T \\ \mathbf{J}_2 & \mathbf{0} \end{bmatrix} \begin{bmatrix} \dfrac{\partial \hat{\mathbf{z}}_k}{\partial \epsilon_k} \\ \dfrac{\partial \hat{\lambda}}{\partial \epsilon_k} \end{bmatrix} = \begin{bmatrix} \mathbf{J}_1^T\mathbf{V}^{-1} \\ \mathbf{0} \end{bmatrix}. \tag{31}$$

Note that the Gauss–Newton approximated Hessian $\mathbf{H} = \mathbf{J}_1^T\mathbf{V}\mathbf{J}_1$ is positive definite for the considered MHE problem (21). The dependence of $\hat{\mathbf{z}}_k$ and $\hat{\lambda}$ on $\mathcal{I}_k^0$ and $\epsilon_k$ is omitted hereafter for the sake of brevity. We assume that the linear independence constraint qualification (LICQ) and sufficient second-order condition hold (see [39, Definition 12.4 and Sec. 12.5]. Then the invertibility of $\mathbf{J}_2\mathbf{H}^{-1}\mathbf{J}_2^T$ is ensured, and (31) can solved by using inversion of block matrices to compute the fault sensitivity of the estimate $\hat{\mathbf{z}}_k$

$$\frac{\partial \hat{\mathbf{z}}_k}{\partial \epsilon_k} = \mathbf{X}\mathbf{J}_1^T\mathbf{V}^{-1} \tag{32}$$

with

$$\mathbf{X} = \mathbf{H}^{-1} - \mathbf{H}^{-1}\mathbf{J}_2^T\big(\mathbf{J}_2\mathbf{H}^{-1}\mathbf{J}_2^T\big)^{-1}\mathbf{J}_2\mathbf{H}^{-1}. \tag{33}$$

To further derive the fault sensitivity of the residual $\mathbf{r}_{k+1}(\mathcal{I}_{k+1}^0, \epsilon_k, \mathbf{f}_{k+1})$ in (29), we use the notation $\hat{\mathbf{z}}_k(\mathcal{I}_k)$ in (27) instead of $\hat{\mathbf{z}}_k(\mathcal{I}_k^0, \epsilon_k)$ in (28) to express the one-step-ahead output prediction $\hat{\mathbf{y}}_{k+1|k}$ in (29). Define $\hat{\mathcal{I}}_k = F_1(\hat{\mathbf{z}}_k(\mathcal{I}_k))$, and then we have $\hat{\mathbf{z}}_k(\mathcal{I}_k) = \hat{\mathbf{z}}_k(\hat{\mathcal{I}}_k)$ according to (28). From (20d) and (21b), the output prediction $\hat{\mathbf{y}}_{k+1|k}$ can be expressed by

$$\begin{aligned} \hat{\mathbf{y}}_{k+1|k} &= h(F(\mathbf{P}_s\hat{\mathbf{z}}_k(\mathcal{I}_k), \mathbf{0}, \Theta_k), \Theta_{k+1}) \\ &= h(F(\mathbf{P}_s\hat{\mathbf{z}}_k(\hat{\mathcal{I}}_k), \mathbf{0}, \Theta_k), \Theta_{k+1}) \\ &= \nu(\hat{\mathcal{I}}_k, \Theta_k, \Theta_{k+1}) \\ &= \nu(F_1(\hat{\mathbf{z}}_k(\mathcal{I}_k)), \Theta_k, \Theta_{k+1}). \end{aligned} \tag{34}$$

In the above-mentioned equation, the function $\nu(\cdot)$ describes how the output prediction relies on $\hat{\mathcal{I}}_k$, and we define

$$\Phi = \tfrac{\partial \nu}{\partial \hat{\mathcal{I}}_k}. \tag{35}$$

With $\mathcal{I}_k = \mathcal{I}_k^0 + \epsilon_k$, $(\partial \hat{\mathbf{z}}_k/\partial \epsilon_k)$ in (32), $\hat{\mathbf{y}}_{k+1|k}$ in (34), and $\Phi$ defined in (35), the fault sensitivity of the residual signal (29) can be obtained as

$$\begin{aligned} \mathbf{S}_f &= \frac{\partial \mathbf{r}_{k+1}}{\partial(\epsilon_k, \mathbf{f}_{k+1})} = \begin{bmatrix} \dfrac{\partial \mathbf{r}_{k+1}}{\partial \epsilon_k} & \dfrac{\partial \mathbf{r}_{k+1}}{\partial \mathbf{f}_{k+1}} \end{bmatrix} \\ &= \begin{bmatrix} -\dfrac{\partial \nu}{\partial \hat{\mathcal{I}}_k}\dfrac{\partial F_1}{\partial \hat{z}_k}\dfrac{\partial \hat{z}_k}{\partial \epsilon_k} & \mathbf{I} \end{bmatrix} = \begin{bmatrix} -\Phi\mathbf{J}_1\mathbf{X}\mathbf{J}_1^T\mathbf{V}^{-1} & \mathbf{I} \end{bmatrix} \\ &= [\Phi \quad \mathbf{I}] \begin{bmatrix} \mathbf{V} - \mathbf{J}_1\mathbf{X}\mathbf{J}_1^T & \mathbf{0} \\ \mathbf{0} & \mathbf{I} \end{bmatrix} \begin{bmatrix} \mathbf{V}^{-1} & \mathbf{0} \\ -\Phi & \mathbf{I} \end{bmatrix}. \end{aligned} \tag{36}$$

Different from the fused healthy measurements $\bar{\mathbf{y}}_{m,k}$ used in the MHE problem (21), the original output measurements $\mathbf{y}_{m,k+1}$ in (1) are used in residual generation (29). For the sake of notational simplicity, the complete output vector $\mathbf{y}_{m,k+1}$ is used. If the residual signal of particular sensor(s), e.g., AOA or VCAS, is of interest, then the corresponding rows of $\mathbf{r}_{k+1}$ in the above-mentioned theorem are selected. In this case, all analysis in Section IV remains the same except that $\Phi$ changes according to the selected output components.

### *B. Fault Sensitivity of Constrained-MHE-Based Residual*

When the faults are too small to activate any inequality constraints, fault sensitivity of the CMHE-FTE is the same as that of the UMHE-FTE. Next, we will show that the improved fault sensitivity of the CMHE-FTE is attributed to the active inequality constraints caused by sufficiently large faults. In this case, we let $\hat{\mathbf{z}}_k^a$ and $\mathbf{r}_{k+1}^a$ denote the estimate and the residual signal in the presence of the active inequality constraints $F_a(\mathbf{z}_k) \leq \mathbf{0}$. Then the KKT condition (31) becomes

$$\begin{bmatrix} \mathbf{H} & \mathbf{J}_2^T & \mathbf{J}_a^T \\ \mathbf{J}_2 & \mathbf{0} & \mathbf{0} \\ \mathbf{J}_a & \mathbf{0} & \mathbf{0} \end{bmatrix} \begin{bmatrix} \dfrac{\partial \hat{\mathbf{z}}_k^a}{\partial \epsilon_k} \\ \dfrac{\partial \hat{\lambda}}{\partial \epsilon_k} \\ \dfrac{\partial \hat{\mu}_a}{\partial \epsilon_k} \end{bmatrix} = \begin{bmatrix} \mathbf{J}_1^T\mathbf{V}^{-1} \\ \mathbf{0} \\ \mathbf{0} \end{bmatrix} \tag{37}$$

where $\mathbf{J}_a^T(\mathbf{z}_k) = (\partial F_a(\mathbf{z}_k)/\partial \mathbf{z}_k)$ and $\mu_a$ represents the Lagrange multiplier of the active inequality constraints. Again by applying the inverse of block matrices to (37), we obtain the fault sensitivity of the estimate and the residual signal in the presence of active inequality constraints

$$\frac{\partial \hat{\mathbf{z}}_k^a}{\partial \epsilon_k} = \mathbf{X}_a\mathbf{J}_1^T\mathbf{V}^{-1} \tag{38}$$

$$\begin{aligned} \mathbf{S}_f^a &= \frac{\partial \mathbf{r}_{k+1}^a}{\partial(\epsilon_k, \mathbf{f}_{k+1})} \\ &= [\Phi \quad \mathbf{I}] \begin{bmatrix} \mathbf{V} - \mathbf{J}_1\mathbf{X}_a\mathbf{J}_1^T & \mathbf{0} \\ \mathbf{0} & \mathbf{I} \end{bmatrix} \begin{bmatrix} \mathbf{V}^{-1} & \mathbf{0} \\ -\Phi & \mathbf{I} \end{bmatrix} \end{aligned} \tag{39}$$

with

$$\mathbf{X}_a = \mathbf{H}^{-1} - \mathbf{H}^{-1}\mathbf{J}_{2a}^T\big(\mathbf{J}_{2a}\mathbf{H}^{-1}\mathbf{J}_{2a}^T\big)^{-1}\mathbf{J}_{2a}\mathbf{H}^{-1} \tag{40}$$

$$\mathbf{J}_{2a} = \begin{bmatrix} \mathbf{J}_2^T & \mathbf{J}_a^T \end{bmatrix}^T \tag{41}$$

which are in the same form as (32) and (36), respectively.

Given the same fault vector $\epsilon_{k+1}$, the estimate $\hat{\mathbf{z}}_k$ from the UMHE and the estimate $\hat{\mathbf{z}}_k^a$ from the CMHE are the same before the inequality constraints become active. It should be noted that $\hat{\mathbf{z}}_k$ deviates from $\hat{\mathbf{z}}_k^a$ after any inequality constraints in the CMHE remain active due to the presence of faults. In this case, the Jacobian $\mathbf{J}_i(\hat{\mathbf{z}}_k)$ in the UMHE is not equal to $\mathbf{J}_i(\hat{\mathbf{z}}_k^a)$ in the CMHE, $i = 1$ or 2, which makes the comparison of the two fault sensitivities not fair. To circumvent this problem, we make the comparison at the same estimate, i.e., $\hat{\mathbf{z}}_k = \hat{\mathbf{z}}_k^a$ at the very first instant that the inequality constraints become active, in the following theorem.

*Theorem 1:* Assume that LICQ and sufficient second-order condition hold before and after sensor faults occur, and additional inequality constraints become active in the presence of faults. In the neighborhood of the same estimate $\hat{\mathbf{z}}_k = \hat{\mathbf{z}}_k^a$ from the UMHE and CMHE, we have $\mathbf{S}_f^a(\mathbf{S}_f^a)^T \geq \mathbf{S}_f\mathbf{S}_f^T$, i.e., improved fault sensitivity of the CMHE-FTE compared to the UMHE-FTE. Besides, a larger number of active inequality constraints lead to higher fault sensitivity.

The proof is given in the Appendix.

## V. Real-Time MHE Algorithm and Its Implementation

In this section, we will discuss the implementation of our proposed CMHE-based FTE method using the Airbus SAO library for industrial V&V purposes. For the nonlinear programming problem (21), we adopt the generalized Gauss–Newton (GGN) SQP strategy and use an efficient structure-exploiting IP algorithm to solve each quadratic programming (QP) subproblem. To achieve real-time computation within a short sampling interval, we perform only one SQP iteration per sample and fix the number of iterations in solving each QP subproblem. This real-time iteration strategy, which has been reported in the literature (see [40]), admits suboptimality of the solution to enable fixed computational cost per sample.

### A. Generalized Gauss–Newton SQP

For the current time horizon $[l, k]$, the original problem (21) is first linearized by applying the GGN SQP strategy, around the solution $\hat{\mathbf{x}}_{i|k-1}$ $(i = l, \cdots, k)$ and $\hat{\mathbf{u}}_{i|k-1}$ $(i = l, \cdots, k-1)$ over the previous time horizon $[l-1, k-1]$. Note that $\hat{\mathbf{x}}_{k|k-1} = F(\hat{\mathbf{x}}_{k-1|k-1}, \hat{\mathbf{u}}_{k-1|k-1}, \Theta_{k-1})$ is the predicted estimate at time instant $k-1$. This leads to the following QP subproblem:

$$\min_{\Delta\mathbf{x}_i, \Delta\mathbf{u}_i} \quad \frac{1}{2}\|\Delta\mathbf{x}_l\|^2_{\mathbf{P}^{-1}} + \frac{1}{2}\sum_{i=l}^{k-1}\|\mathbf{r}_{u,i} - \Delta\mathbf{u}_i\|^2_{\mathbf{Q}^{-1}} \tag{42a}$$

$$+ \frac{1}{2}\sum_{i=l}^{k}\|\mathbf{r}_{y,i} - \mathbf{C}_i\Delta\mathbf{x}_i\|^2_{\mathbf{R}^{-1}}$$

$$\text{s.t. } \Delta\mathbf{x}_{i+1} = \mathbf{f}_i + \mathbf{A}_i\Delta\mathbf{x}_i + \mathbf{B}_i\Delta\mathbf{u}_i$$

$$\Delta\mathbf{u}_i^{\text{LB}} \leq \Delta\mathbf{u}_i \leq \Delta\mathbf{u}_i^{\text{UB}}, \quad i = l, \ldots, k-1$$

$$\Delta\mathbf{x}_i^{\text{LB}} \leq \Delta\mathbf{x}_i \leq \Delta\mathbf{x}_i^{\text{UB}}, \quad i = l, \ldots, k \tag{42b}$$

where

$$\mathbf{x}_{l|k}^{-} = \hat{\mathbf{x}}_{l|k-1}, \quad \Delta\mathbf{x}_i = \mathbf{x}_i - \hat{\mathbf{x}}_{i|k-1}, \ \Delta\mathbf{u}_i = \mathbf{u}_i - \hat{\mathbf{u}}_{i|k-1}$$
$$\mathbf{r}_{u,i} = -\hat{\mathbf{u}}_{i|k-1}, \ \mathbf{r}_{y,i} = \bar{\mathbf{y}}_{m,i} - h(\hat{\mathbf{x}}_{i|k-1}, \Theta_i)$$
$$\mathbf{A}_i = \nabla_{\mathbf{x}}F(\hat{\mathbf{x}}_{i|k-1}, \hat{\mathbf{u}}_{i|k-1}, \Theta_i)$$
$$\mathbf{B}_i = \nabla_{\mathbf{u}}F(\hat{\mathbf{x}}_{i|k-1}, \hat{\mathbf{u}}_{i|k-1}, \Theta_i)$$
$$\mathbf{C}_i = \nabla_{\mathbf{x}}h(\hat{\mathbf{x}}_{i|k-1}, \Theta_i)$$
$$\mathbf{f}_i = \hat{\mathbf{x}}_{i|k-1} - \hat{\mathbf{x}}_{i+1|k-1} + t_s F(\hat{\mathbf{x}}_{i|k-1}, \hat{\mathbf{u}}_{i|k-1}, \Theta_i)$$
$$\Delta\mathbf{u}_i^{\text{LB}} = \mathbf{u}_i^{\text{LB}} - \hat{\mathbf{u}}_{i|k-1}, \quad \Delta\mathbf{u}_i^{\text{UB}} = \mathbf{u}_i^{\text{UB}} - \hat{\mathbf{u}}_{i|k-1}$$
$$\Delta\mathbf{x}_i^{\text{LB}} = \mathbf{x}_i^{\text{LB}} - \hat{\mathbf{x}}_{i|k-1}, \quad \Delta\mathbf{x}_i^{\text{UB}} = \mathbf{x}_i^{\text{UB}} - \hat{\mathbf{x}}_{i|k-1}.$$

Its solution $\{\Delta\mathbf{x}_{i|k}, \Delta\mathbf{u}_{i|k}\}$ is computed using the algorithm given in Section V-B. Finally, the solution to the original problem (21) is updated as $\hat{\mathbf{x}}_{i|k} = \hat{\mathbf{x}}_{i|k-1} + \Delta\mathbf{x}_{i|k}$ and $\hat{\mathbf{u}}_{i|k} = \hat{\mathbf{u}}_{i|k-1} + \Delta\mathbf{u}_{i|k}$, and used to initialize the SQP iteration at the next time instant.

### B. Solving the QP Subproblem

An infeasible start primal barrier IP method is adopted to solve the QP subproblem (42). We first replace the inequality constraints in the QP (42) with barrier terms in its objective function, to get the approximate problem [39], [41], [42]

$$\min_{\Delta\mathbf{x}_i, \Delta\mathbf{u}_i} \quad \frac{1}{2}\|\Delta\mathbf{x}_l\|^2_{\mathbf{P}^{-1}} + \frac{1}{2}\sum_{i=l}^{k-1}\|\mathbf{r}_{u,i} - \Delta\mathbf{u}_i\|^2_{\mathbf{Q}^{-1}}$$

$$+ \frac{1}{2}\sum_{i=l}^{k}\|\mathbf{r}_{y,i} - \mathbf{C}_i\Delta\mathbf{x}_i\|^2_{\mathbf{R}_i^{-1}} + \kappa\phi(\Delta\mathbf{u}, \Delta\mathbf{x})$$

$$\text{s.t. } \Delta\mathbf{x}_{i+1} = \mathbf{f}_i + \mathbf{A}_i\Delta\mathbf{x}_i + \mathbf{B}_i\Delta\mathbf{u}_i, i = l, \ldots, k-1 \tag{43}$$

where $\kappa > 0$ is a barrier parameter, and the function $\phi(\cdot)$ is the log barrier defined as

$$\phi(\Delta\mathbf{u}, \Delta\mathbf{x}) = \sum_{i=l}^{k-1}\sum_{j=1}^{n_u}\phi_u(\Delta\mathbf{u}_i(j)) + \sum_{i=l}^{k}\sum_{j=1}^{A_x}\phi_x(\Delta\mathbf{x}_i(j))$$

$$\phi_\star(\Delta\star_i(j)) = -\log\left(\Delta\star_i^{\text{UB}}(j) - \Delta\star_i(j)\right) - \log\left(\Delta\star_i(j) - \Delta\star_i^{\text{LB}}(j)\right) \tag{44}$$

with $\star$ representing $\mathbf{u}$ and $\mathbf{x}$, and $j$ referring to the $j$th entry of the vector $\star$. A sequence of the approximate problems (43) are solved iteratively for a decreasing sequence of values of $\kappa$, as described in Algorithm 1. For real-time computation, the number of the $\kappa$ values in the sequence is fixed to $n_\kappa$, and we perform $n_{QP}$ iterations for each approximate problem (43) with a particular value of $\kappa$. A simple backtracking line search is used to ensure that the inequality constraints are satisfied at all iterations.

At each iteration in Algorithm 1, the KKT system of the approximate problem (43) is linearized and solved to compute the search direction represented by $\Delta^2\mathbf{x}_i$ and $\Delta^2\mathbf{u}_i$, $i = l, \cdots, k$. Such a linearized KKT system is equivalent to the KKT condition of the following linear MHE problem with only equality constraints, omitting detailed explanations for the sake of brevity

$$\min_{\Delta^2\mathbf{x}_i, \Delta^2\mathbf{u}_i} \quad \frac{1}{2}\|\bar{\mathbf{r}}_x - \Delta^2\mathbf{x}_l\|^2_{\mathbf{P}^{-1}} + \frac{1}{2}\sum_{i=l}^{k-1}\|\bar{\mathbf{r}}_{u,i} - \Delta^2\mathbf{u}_i\|^2_{\bar{\mathbf{Q}}_i^{-1}}$$

$$+ \frac{1}{2}\sum_{i=l}^{k}\|\bar{\mathbf{r}}_{y,i} - \bar{\mathbf{C}}_i\Delta^2\mathbf{x}_i\|^2_{\bar{\mathbf{R}}_i^{-1}}$$

$$\text{s.t. } \Delta^2\mathbf{x}_{i+1} = -\mathbf{r}_{p,i} + \mathbf{A}_i\Delta^2\mathbf{x}_i + \mathbf{B}_i\Delta^2\mathbf{u}_i$$

$$i = l, \ldots, k-1 \tag{45}$$

**Algorithm 1** Primal Barrier IP Algorithm

*Initialization*: $\kappa = \kappa_{\text{init}}$, $\{\Delta\mathbf{x}_i^- = 0, \Delta\mathbf{u}_i^- = 0\}_{i=l,\cdots,k}$.
**for** $j = 0 \to n_\kappa n_{QP} - 1$ **do**
*Linearization*: compute all the quantities in (46).
*Compute the search direction* $\{\Delta^2\mathbf{x}_i, \Delta^2\mathbf{u}_i\}_{i=l,\cdots,k}$ with Algorithm 2.
*Line search*:

$$s_j = \max\left\{ 2^{-n_s} \;\middle|\; \begin{array}{l} \Delta\star_i^{\text{LB}} \le \eta_{\star,i}(2^{-n_s}) \le \Delta\star_i^{\text{UB}}, \\ i = l, \cdots, k, \text{and } n_s \le n_s^{\max} \\ \text{is a nonnegative integer} \end{array} \right\}$$

where $\eta_{\star,i}(\mu) = \Delta\star_i^- + \mu\Delta^2\star_i$ with $\star$ representing $\mathbf{u}$ and $\mathbf{x}$. $s_j$ is set to zero if there does not exist a nonnegative integer $n_s < n_s^{\max}$ that satisfies all the inequality constraints.
*Update*:
$(\Delta\mathbf{x}_i^-, \Delta\mathbf{u}_i^-) \leftarrow (\Delta\mathbf{x}_i^-, \Delta\mathbf{u}_i^-) + s_j(\Delta^2\mathbf{x}_i, \Delta^2\mathbf{u}_i)$,
$\kappa \leftarrow 0.1\kappa$ if $j$ is an integral multiple of $n_\kappa$.
**end for**
*Solution* to the QP (42): $\left(\Delta\mathbf{x}_{i|k}, \Delta\mathbf{u}_{i|k}\right) \leftarrow \left(\Delta\mathbf{x}_i^-, \Delta\mathbf{u}_i^-\right)$.

where we define

$$\mathbf{g}_{\star,i} = \text{vect}\left(\left\{\nabla\phi_\star\left(\Delta\star_i^-(j)\right)\right\}_{j=1,2,3}\right) \tag{46a}$$

$$\mathbf{L}_{\star,i} = \text{diag}\left(\left\{\sqrt{\nabla^2\phi_\star(\Delta\star_i^-(j))}\right\}_{j=1,2,3}\right), \quad \text{with } \star \text{ being } \mathbf{u} \text{ and } \mathbf{x} \tag{46b}$$

$$\mathbf{r}_{p,i} = -\mathbf{f}_i - \mathbf{A}_i\Delta\mathbf{x}_i^- - \mathbf{B}_i\Delta\mathbf{u}_i^- + \Delta\mathbf{x}_{i+1}^- \tag{46c}$$

$$\bar{\mathbf{r}}_x = -\Delta\mathbf{x}_l^-, \bar{\mathbf{r}}_{u,i} = \mathbf{Q}^{-1}\left(\mathbf{r}_{u,i} - \Delta\mathbf{u}_i^-\right) - \kappa\mathbf{g}_{u,i} \tag{46d}$$

$$\bar{\mathbf{r}}_{y,i} = \begin{bmatrix} \mathbf{r}_{y,i} - \mathbf{C}_i\Delta\mathbf{x}_l^- \\ -\sqrt{\kappa}\mathbf{L}_{x,i}^{-1}\mathbf{g}_{x,i} \end{bmatrix}, \quad \bar{\mathbf{C}}_i = \begin{bmatrix} \mathbf{C}_i \\ \sqrt{\kappa}\mathbf{L}_{x,i} \end{bmatrix} \tag{46e}$$

$$\bar{\mathbf{R}}_i = \text{diag}(\mathbf{R}_i, \mathbf{I}_{A_x}), \quad \bar{\mathbf{Q}}_i = \left(\mathbf{Q}^{-1} + \kappa\mathbf{L}_{u,i}^T\mathbf{L}_{u,i}\right)^{-1}. \tag{46f}$$

Note that vect($\{x(i)\}$) and diag($\{x(i)\}$) in (46a) and (46b) represent a column vector and a diagonal matrix, respectively, with scalar entries $\{x(i)\}$. Because of the above-mentioned equivalence, the linearized KKT system of (43) is solved by applying a structure-exploiting Riccati-based algorithm on the linear UMHE problem (46), which is inspired by [42, Ch. 4] and detailed in Algorithm 2. In each iteration of Algorithm 1, solving the search direction by Algorithm 2 is the most expensive step whose computational complexity is $O(N(n_x + n_u)^3)$, with $n_x$ and $n_u$ denoting dimensions of the state $\mathbf{x}_i$ and the unknown input $\mathbf{u}_i$, respectively [42].

### C. Implementation Aspects

In the RECONFIGURE project, the implementation using SAO is a critical step to assess the feasibility of real-time computation on FCCs. The following aspects have been considered to either speed up computation or simplify the implementation while maintaining good estimation performance.

The overall computational cost is kept small by setting the horizon length $N$ of the MHE problem (21) to be three. Further increasing the estimation horizon length does not necessarily improve the estimation performance, since more

**Algorithm 2** Solve the Search Direction

*Riccati recursion based factorization*:
$\hat{\mathbf{P}}_l = \mathbf{P}$
**for** $i = l \to k$ **do**
  $\Pi_i \leftarrow \bar{\mathbf{C}}_i\hat{\mathbf{P}}_i,\ \Xi_i \leftarrow \left(\bar{\mathbf{R}}_i + \Pi_i\bar{\mathbf{C}}_i^{\text{T}}\right)^{-1},\ \Omega_i \leftarrow \bar{\mathbf{C}}_i^{\text{T}}\Xi_i$
  $\mathbf{K}_i \leftarrow \hat{\mathbf{P}}_i\Omega_i,\ \mathbf{P}_i^f \leftarrow \hat{\mathbf{P}}_i - \mathbf{K}_i\Pi_i$
  **if** $i < k$ **then**
    $\hat{\mathbf{P}}_{i+1} \leftarrow \mathbf{A}_i\mathbf{P}_i^f\mathbf{A}_i^{\text{T}} + \mathbf{B}_i\bar{\mathbf{Q}}_i\mathbf{B}_i^{\text{T}}$
  **end if**
**end for**
*Forward recursion*:
$\Delta^2\hat{\mathbf{x}}_l = \bar{\mathbf{r}}_x$
**for** $i = l \to k$ **do**
  $\breve{\mathbf{r}}_i \leftarrow \bar{\mathbf{r}}_{y,i} - \bar{\mathbf{C}}_i\Delta^2\hat{\mathbf{x}}_i,\ \Delta^2\mathbf{x}'_i \leftarrow \Delta^2\hat{\mathbf{x}}_i + \mathbf{K}_i\breve{\mathbf{r}}_i$
  **if** $i < k$ **then**
    $\Delta^2\mathbf{u}'_i \leftarrow \bar{\mathbf{r}}_{u,i}$
    $\Delta^2\hat{\mathbf{x}}_{i+1} \leftarrow -\mathbf{r}_{p,i} + \mathbf{A}_i\Delta^2\mathbf{x}'_i + \mathbf{B}_i\Delta^2\mathbf{u}'_i$
  **end if**
**end for**
*Backward recursion*:
$\Delta^2\mathbf{x}_k \leftarrow \Delta^2\mathbf{x}'_k,\ \lambda_{k-1} \leftarrow -\Omega_k\breve{\mathbf{r}}_k$
**for** $i = k-1 \to 0$ **do**
  $\xi_i \leftarrow \mathbf{A}_i^{\text{T}}\lambda_i,\ \Delta^2\mathbf{u}_i \leftarrow \Delta^2\mathbf{u}'_i - \bar{\mathbf{Q}}_i\mathbf{B}_i^{\text{T}}\lambda_i$
  $\Delta^2\mathbf{x}_i \leftarrow \Delta^2\mathbf{x}'_i - \mathbf{P}_i^f\xi_i$
  **if** $i > 0$ **then**
    $\lambda_{i-1} \leftarrow \xi_i - \Omega_i\left(\breve{\mathbf{r}}_i + \Pi_i\xi_i\right)$
  **end if**
**end for**

wind disturbances and measurement noises are included within the horizon. For the purpose of noise filtering in the residual signal, the length $N_{\text{eval}}$ of the residual evaluation window in (18) is set to 10, at the cost of slightly increased fault detection delay. The number of iterations $n_\kappa$ and $n_{QP}$ in Algorithm 1 are both fixed to 2, in order to achieve the real-time feasibility on FCCs. Extensive numerical simulations show good results even with such small number of iterations.

As explained in Section III-C, in the configurations II–IV of the output vector used in the proposed MHE algorithm, the AOA or VCAS measurements should not be involved when all redundant AOA or VCAS sensors are identified as faulty. However, this cannot be done by directly removing AOA or VCAS from the output equation (20d), because vectors and matrices of time-varying sizes (which are needed to reconfigure the output equation in the MHE algorithm) are not supported in the SAO library. To simplify the SAO implementation for the above-mentioned issue, we let the output equation (20d) remain the same, but set only the third or fourth row of the matrix $\mathbf{C}_i$ in (42a) to zero after losing all AOA or VCAS sensors, respectively. By doing so, the feedback information from AOA or VCAS becomes ineffective when necessary in one of the configurations II–IV, and the SAO implementation still works with vectors and matrices of fixed sizes. In particular, this allows the MHE implementation to work on the observable subsystem associated with $(\alpha, V_g, W_z)$ and discard the unobservable $W_x$ in the configurations III and IV.

Lookup tables are used to approximate logarithm and power computations involved in $g_{\star,i}$ and $\mathbf{L}_{\star,i}$ in (46) as well as the entries of the fourth row of $\mathbf{C}_i$.

Computing the search direction by solving the linearized KKT system of (43) dominates the computational cost of Algorithm 1. This step follows Algorithm 2 in the SAO implementation by taking the following strategies.

1) The intermediate results, e.g., $\Pi_i$, $\Xi_i$, $\mathbf{\Omega}_i$, $\mathbf{K}_i$ in lines 4 and 5, $\check{\mathbf{r}}_i$ in line 13, and $\xi_i$ in line 22 of Algorithm 2, are reused in subsequent computations.
2) The symmetric or diagonal matrix structures are exploited in all the matrix manipulations.
3) To compute $\Xi_i$ in line 4 of Algorithm 2, the block matrix inversion formula is applied so that the inversion of the matrix $\bar{\mathbf{R}}_i + \Pi_i \bar{\mathbf{C}}_i^T$ can be reduced to the inversion of several matrices of smaller size that is computed via the analytical adjugate formula.

With all the above-mentioned efforts, the real-time computational cost of our SAO implementation is 5.8-ms per sample under the industrial assessment performed by Airbus. This highlights the feasibility of applying online optimization-based MHE methods on FCCs, although it is still computationally significant from the perspective of an aircraft application.

## VI. Simulation Results

In this section, the Functional Engineering Simulation environment [1], [27] is used to test the proposed CMHE-FTE approach. We first illustrate its benefits by comprisons with the EKF-based FTE (EKF-FTE) and the UMHE-FTE, and then evaluate its effectiveness using multiple parametric runs over a wide range of the flight envelop during different maneuvers.

### *A. Comparison Between the EKF, UMHE, and CMHE-Based FTE*

We compare the proposed CMHE-FTE with conventional unconstrained FTE in terms of robustness to disturbances and sensitivity to faults. In order to illustrate the effect of inequality constraints incorporated in the CMHE-FTE, we use EKF and UMHE in Step 3 of the proposed FTE scheme shown in Fig. 1 for comparisons. As discussed in Section IV-A, the only difference from the CMHE-FTE in the UMHE-FTE lies in the absence of inequality constraints. In the MHE problem (21) and (22), the weighting matrices $\mathbf{P}$, $\mathbf{Q}$, and $\mathbf{R}$ are determined by the relative belief in the *a priori* estimate $\mathbf{x}_{l|k}^-$, the dynamic equation in (21b), and the output equation in (20d), respectively. To be specific, $R_\alpha$, $R_{vz}$, and $R_{vc}$ in $\mathbf{R}$ are set to be the measurement noise variances. The weights $q_\alpha$, $q_v$, and $q_w$ in $\mathbf{Q}$ are determined by the variances of the lumped disturbances in (21b) caused by winds and model approximation errors. The weight $p_\alpha$ is set to be smaller (or larger) than $R_\alpha$ if there is higher (or lower) belief in the a priori AOA estimates than in the AOA measurements. The same rule applies to the weight $p_v$ with regard to $R_{vc}$. From the FDI point of view, $p_w$ and $q_w$ have an additional role for a tradeoff between fault sensitivity and disturbance robustness, as discussed later in this section. The weighting matrices $\mathbf{Q}$ and $\mathbf{R}$ in (21) are used as the covariance matrices in the EKF, in order to ensure a fair comparison with the UMHE and the CMHE. Other $\mathcal{H}_i/\mathcal{H}_\infty$ fault detection filters [43] are not used in the comparisons because they consider only the FDI performance without providing reliable state estimates. All the simulation runs in this subsection are conducted at a speed of 350 kts and an altitude of 5000 ft.

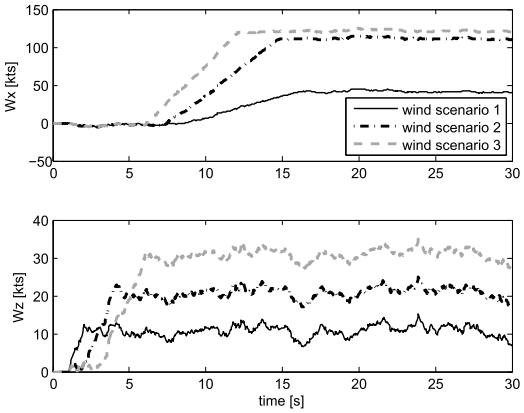


Fig. 2. Three wind scenarios used to compare the EKF-FTE, UMHE-FTE, and CMHE-FTE.

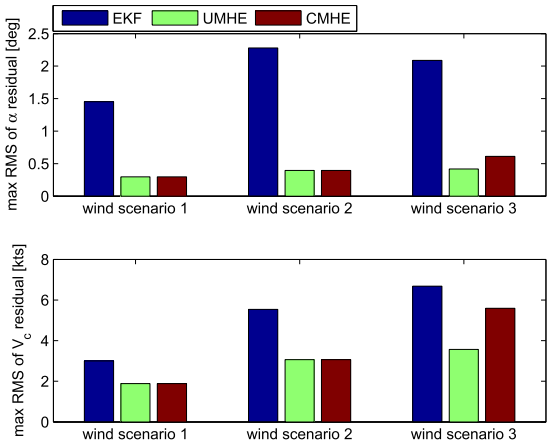


Fig. 3. Comparison of robustness to disturbances of the EKF-FTE, UMHE-FTE, and CMHE-FTE in different wind scenarios without faults: maximum rms of the residuals for AOA and VCAS with $p_w = 0.01$ and $q_w = 0.1$.

*1) Robustness to Disturbance:* First, we compare the EKF-FTE, UMHE-FTE, and CMHE-FTE in terms of the disturbance robustness. For given wind disturbances, disturbance robustness can be measured by maximum rms of the residuals for AOA and VCAS, i.e., (18), in the absence of faults: smaller rms of the residual implies higher robustness to disturbances. We test the above-mentioned three FTE methods under three wind scenarios shown in Fig. 2. As illustrated in Fig. 3, with the same tuning parameters, the size of the residual signals in each method generally grows with the size of the wind disturbances. Under wind scenarios 1 and 2, the fault-free residual signals of the EKF-FTE are less robust than the UMHE-FTE and the CMHE-FTE, while the residual signals of the UMHE-FTE and the CMHE-FTE have almost the same size, because no inequality constraints are active in both wind scenarios when solving (21). However, the wind amplitudes in wind scenario 3 are larger than the assumed bounds of winds in the CMHE-FTE, which activates the inequality constraints in the CMHE-FTE. Therefore, the residual signals of the

CMHE-FTE become larger than those of the UMHE-FTE in wind scenario 3. From the results under all three wind scenarios, we can see that the UMHE-FTE and the CMHE-FTE have almost the same robustness to disturbances when the real winds are within their assumed bounds in the CMHE-FTE, while the CMHE-FTE becomes less robust to disturbances than the UMHE-FTE when the real winds are larger than their assumed bounds. This shows that the wind bounds used in the CMHE-FTE need to be properly selected according to the weather and flight conditions.

In the above-mentioned fault-free simulations, the EKF-FTE gives much larger estimation error than the UMHE-FTE and the CMHE-FTE, and we need larger thresholds to ensure zero false alarms when using the EKF-FTE. Thus, under the condition of zero false alarm, the EKF-FTE is less sensitive to faults than the UMHE-FTE and the CMHE-FTE with suitably predefined bounds of winds.

*2) Benefit of Incorporating Inequality Constraints:* Next, we illustrate the benefit of incorporating inequality constraints by comparing the UMHE-FTE and the CMHE-FTE in the case of three simultaneous VCAS sensor faults. All AOA sensors are assumed healthy, and thus only the detection of VCAS sensor faults is discussed. Both the UMHE-FTE and CMHE-FTE include the AWF strategy, and their detection thresholds are set to be the same. As shown in Fig. 4(c)–(f), the UMHE-FTE compensates for the VCAS sensor faults in its horizontal wind estimate, and thus the size of its residual signal fails to trigger the detection threshold. This shows the ineffectiveness of the AWF strategy in the presence of three simultaneous VCAS sensor faults, although it improves fault sensitivity for less than three VCAS sensor faults, as explained in Section III-A. In contrast, as shown in Fig. 4(c), at about 24 s, the horizontal wind estimate of the CMHE-FTE reaches its upper bound for the first time, and meanwhile, it is still equal to the unconstrained horizontal wind estimate. Fig. 4(d)–(f) further shows that at this very time instant, the fault sensitivity of the constrained residuals is significantly higher than that of the unconstrained residuals, which is proved by Theorem 1. After that, the constrained wind estimates still cannot compensate for the fault effects since its upper bound remain active. This leads to the rapid growth of its residual signal with about 4-s delay after the fault occurrence. Due to the observability issue explained in Section III-C, the VCAS estimates become unreliable after removing all three faulty VCAS sensors, as in Fig. 4(b). Similar to the UMHE-FTE, the EKF-FTE cannot detect all the three faulty VCAS sensors due to the same reason related to the AWF strategy.

We proceed by repeating the test scenario in Fig. 4 with different runaway rates and tuning parameters to highlight the positive effect of inequality constraints on fault sensitivity. Similar to disturbance robustness, fault sensitivity is not directly evaluated by computing the fault sensitivity matrix $\mathbf{S}_f^a$ in (39), because the active constraints required to compute $\mathbf{S}_f^a$ are unknown before actually solving the problem (21). Here, we indirectly evaluate fault sensitivity by the averaged rms of the residual within 17.76 s (370 data samples) immediately after fault injection. Larger rms of the residual implies higher sensitivity to faults.

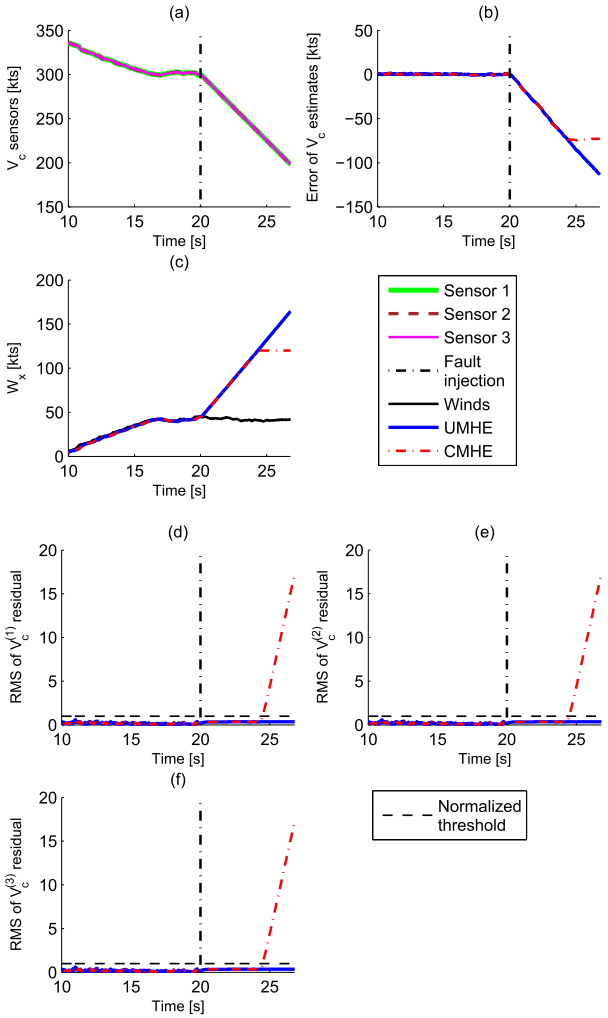


Fig. 4. Comparison of the UMHE-FTE and CMHE-FTE for three simultaneous VCAS runaway faults in wind scenario 1 (runaway rate at $-15$ kts/s and tuning parameters $p_w = 0.01$ and $q_w = 1$). (a) $V_c$ sensor measurements. (b) Errors of $V_c$ estimates. (c) Wind speed and its estimate. (d) Generated residual for $V_c^{(1)}$ sensor. (e) Generated residual for $V_c^{(2)}$ sensor. (f) Generated residual for $V_c^{(3)}$ sensor.

Fig. 5 shows the results of the UMHE-FTE and the CMHE-FTE with different tuning parameters $q_w$ and fixed $p_w = 0.01$. The performance comparisons with different $p_w$ are similar, thus omitted. For runaway rate smaller than 10 kts/s, the CMHE-FTE produces approximately the same rms of the residual as the UMHE-FTE, since the inequality constraints in the CMHE-FTE have become activated for only a very short duration within 17.76 s after fault injection. For runaway rate larger than 10 kts/s, the inequality constraints of the CMHE-FTE quickly become active after fault injection. Therefore, the CMHE-FTE gives significantly larger rms of the residual, which implies higher fault sensitivity, than the UMHE-FTE, given either $q_w = 0.0001$ or $q_w = 1$. Moreover, when $q_w$ increases from 0.0001 to 1, more wind disturbances and a larger portion of fault perturbation can be interpreted by the assumed wind dynamics in (20c), and thus disturbance robustness improves but fault sensitivity decreases. However, it can be seen from Fig. 5(a) that with the same increased $q_w$, the CMHE-FTE suffers much less from the reduction of fault sensitivity than the UMHE-FTE, especially when the runaway rate

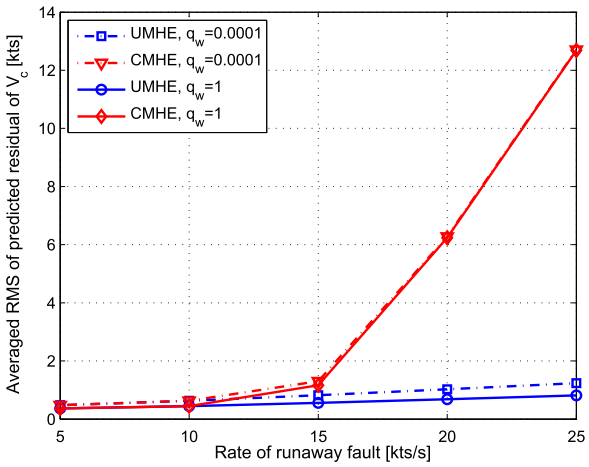


(a)

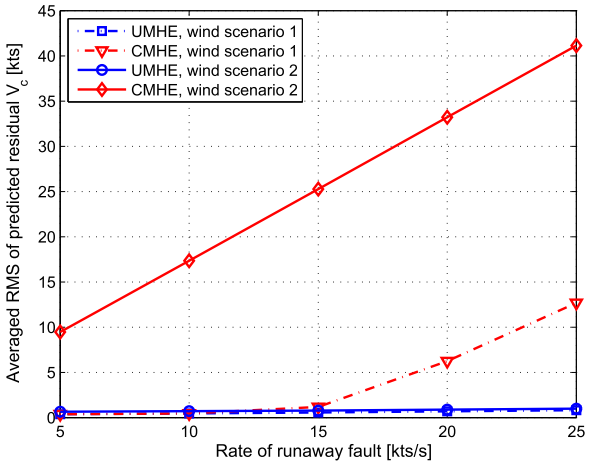


(b)

Fig. 5. Comparison of sensitivity to faults: rms of predicted residual signal for different rates of runaway faults. (a) Wind scenario 1 in Fig. 2, with $p_w = 0.01$ and different $q_w$. (b) Wind scenarios 1 and 2 in Fig. 2, with $p_w = 0.01$ and $q_w = 1$.

is larger than 15 kts/s. The reason is that in the CMHE-FTE, the positive effect of active inequality constraints on fault sensitivity compensates for the negative effect of increasing $q_w$.

To illustrate how the fault sensitivity changes with winds, Fig. 5(b) shows the results of the UMHE-FTE and the CMHE-FTE under two different wind scenarios given in Fig. 2. Even though the wind amplitudes in wind scenario 2 are significantly larger than in wind scenario 1, the averaged rms values of the residuals obtained in the UMHE-FTE do not change much in both wind scenarios. However, for the CMHE-FTE, the inequality constraints of the wind estimates are more easily activated in the presence of faults, when the true wind speed or acceleration is already close to the boundary of the inequality constraints. This leads to the significant increase of averaged residual rms obtained by the CMHE-FTE in wind scenario 2, compared with that in wind scenario 1.

### *B. Parametric Simulation Results*

To further evaluate the proposed CMHE-FTE and its real-time implementation, we performed 249 fault-free and faulty parametric runs that sweep grid parameter dispersions over a wide range of the flight envelop during different maneuvers. Diverse wind profiles are simulated, with the amplitudes of wind speeds and accelerations less than 120 kts and 15 kts/s, respectively, in the vertical, longitudinal, and lateral directions. When the lateral motion caused by the lateral wind is not significant, the effect of lateral motion can be regarded as one source of model mismatches in the longitudinal model (1), which is accounted for by the process noise and the measurement noise. Various types of sensor faults are randomly generated and injected into AOA and VCAS sensors, as shown in Table II. Examples of different types of faults can be found in [13] and [20]. The duration of each parametric run varies from 60 to 700 s. The following metrics are used to evaluate the FDI performance.

TABLE II
FAULT TYPE, AMPLITUDE, RATE, OR FREQUENCY

| Fault type | AOA | VCAS |
|---|---|---|
| Oscillation | 0.5∼25 deg<br>0.5∼1 Hz | 10∼200 kts<br>0.5∼4 Hz |
| Jamming | 0.5∼25 deg | 10∼200 kts |
| Bias | 0.5∼25 deg | 10∼200 kts |
| Runaway | 0.2∼25 deg/s | 0.5∼50 kts/s |
| Non-return to zero | 10% × current value | 10% × current value |
| Noise | Standard deviation<br>1∼2 deg | Standard deviation<br>10∼20 kts |

1) *False Alarm Rate (FAR)*: It is the percentage ratio of fault-free runs where a fault is incorrectly detected.
2) *Miss Detection Rate (MDR)*: It is the percentage ratio of faulty runs where at least one faulty sensor is not detected.
3) *False Isolation Rate (FIR)*: It is the percentage ratio of faulty runs where at least one healthy sensor is incorrectly identified as faulty.
4) *Max Detection Delay (DetD)*: $\max_i \left(t_{i,\text{detect}} - t_{i,\text{fault}}\right)$, where $t_{i,\text{detect}}$ and $t_{i,\text{fault}}$ represent the fault detection time and fault occurrence time of the single run indexed by $i$, respectively.
5) *Mean Detection Delay*: $\text{mean}_i \left(t_{i,\text{detect}} - t_{i,\text{fault}}\right)$.

For the 140 fault-free runs, we get good estimation performance as shown in the first row of Table III. Considering the worst case estimation errors in the fault-free runs, we set the detection threshold to be $J_{\alpha,\text{th}} = 2.9$ deg and $J_{vc,\text{th}} = 12$ kts, which ensures zero FAR in the fault-free scenarios. The 109 faulty runs can be divided into the four categories listed in Table I, with 47, 22, 25, and 15 runs in each fault category, respectively. We get zero MDR, negligible FIR, and very short detection delay in the overall FDI performance statistics as listed in Table IV. The averaged estimation errors in Table III are also small. Note that the VCAS estimates under the configurations III and IV are not included, because the VCAS cannot be reliably reconstructed in these two configurations due to the unobservability issue explained in Section III-C.

Two representative challenging runs are included here to explain the reasons of the worst case detection delays and estimation errors in Tables III and IV. In the first representative run, we have a detection delay of 19.16 s for the jamming AOA sensors, as shown in Fig. 6(a). It can be seen that the jamming

TABLE III
ESTIMATION PERFORMANCE OF PARAMETRIC RUNS

| | Max absolute error | | Mean absolute error | |
|---|---|---|---|---|
| | AOA [deg] | VCAS [kts] | AOA [deg] | VCAS [kts] |
| Fault-free runs | 2.44 | 8.22 | 0.02 | 0.02 |
| Faulty runs | 16.39 | 8.22 | 0.24 | 0.02 |

TABLE IV
FAULT DIAGNOSIS PERFORMANCE OF PARAMETRIC RUNS

| | FAR [%] | MDR [%] | FIR [%] | DetD [s] | |
|---|---|---|---|---|---|
| | | | | max | mean |
| AOA | 0 | 0 | 0.92 | 19.16 | 0.75 |
| VCAS | 0 | 0 | 0 | 4.64 | 0.80 |

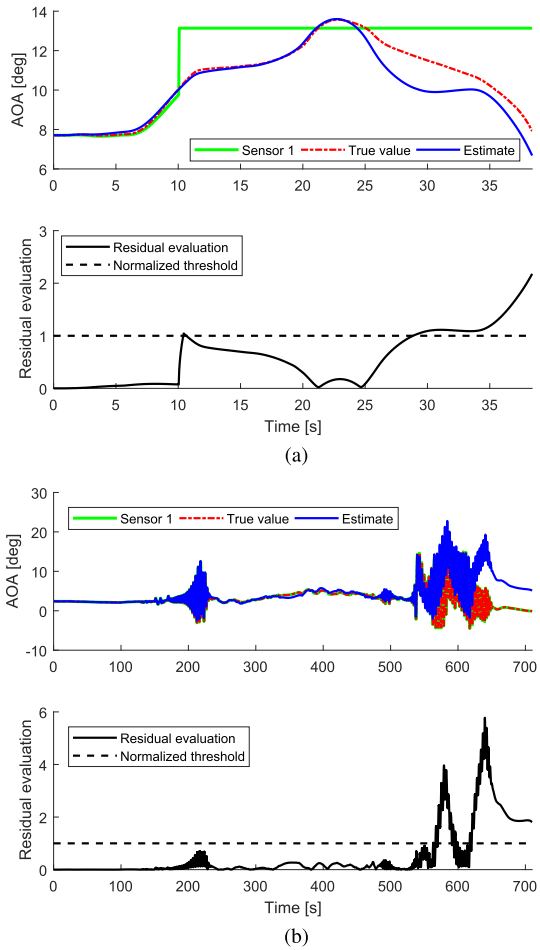


Fig. 6. Results of two representative challenging runs. (a) Jamming faults in two AOA sensors and two VCAS sensors. (b) Fault-free AOA sensors and the faults of nonreturn to zero in three VCAS sensors.

AOA sensor outputs are close to their fault-free values, which keeps the residual rms values below the given detection threshold. Similar reasons lead to the worst case detection delays of the VCAS faults in Table IV. The second representative run is under configuration III of faulty runs. Although the faults of nonreturn to zero in all three VCAS sensors are isolated by our proposed approach, the fault information still propagates via the nominal controller without taking any fault-tolerant control strategy, thus leading to fast transients of the fault-free AOA outputs, as in Fig. 6(b). In the presence of such transients, the worst case absolute estimation error of AOA reaches 16.39°, which results in incorrect fault isolation, as shown in Fig. 6. This problem can be solved by: 1) tuning the threshold and the horizon length of residual evaluation, at the cost of reducing fault detection rate and increasing detection delay or 2) reconfigurable control to account for the VCAS sensor faults, which is not within the scope of this paper. Note that the worst case VCAS estimation errors in Table III are satisfactory compared with the fault-free VCAS measurements in the range from 160 to 360 kts. Dedicated tuning of the weighting matrices, the detection thresholds, and the length of the residual evaluation window can always improve the performance of any particular single run, but it does not necessarily improve the overall performance statistics of multiple runs because of the involved tradeoffs among different performance criteria. This suggests that there are potential benefits of adaptive tuning of more algorithm parameters, which is left to future research.

## VII. CONCLUSION

This paper presented a fault-tolerant MHE approach for combined air data sensor fault diagnosis and estimation. Compared with the conventional unconstrained methods, the proposed constrained fault-tolerant estimator improves the fault sensitivity by incorporating proper wind bounds, without sacrificing robustness to winds. Nonlinear programming sensitivity analysis shows that this benefit applies to general MHE-based residual generators when imposing state constraints. Using an efficient structure-exploiting algorithm within a real-time iteration scheme, the proposed method was implemented with the Airbus graphical symbol library. Its real-time applicability has been successfully validated in an industrial assessment, and it has achieved satisfactory performance over a wide range of the flight envelop when tested in a high-fidelity Airbus simulator. The limitations of using fixed weighting matrices over the entire flight envelop suggest that adaptive tuning of more algorithm parameters is a promising direction to improve the overall diagnosis and estimation performance.

## APPENDIX
## PROOF OF THEOREM 1

With the same estimate $\hat{\mathbf{z}}_k = \hat{\mathbf{z}}_k^a$, the UMHE and CMHE have the same $\Psi$, $\mathbf{J}_1$, $\mathbf{J}_2$, and $\mathbf{H}$. Let the symmetric matrix $\Pi$ denote the matrix square root of the Hessian matrix $\mathbf{H}$, i.e., $\mathbf{H} = \Pi \cdot \Pi$, and define

$$\mathcal{P} = \mathbf{I} - \Pi^{-1}\mathbf{J}_2^T\left(\mathbf{J}_2\Pi^{-2}\mathbf{J}_2^T\right)^{-1}\mathbf{J}_2\Pi^{-1} \tag{47}$$

$$\mathcal{P}_a = \mathbf{I} - \Pi^{-1}\mathbf{J}_{2a}^T\left(\mathbf{J}_{2a}\Pi^{-2}\mathbf{J}_{2a}^T\right)^{-1}\mathbf{J}_{2a}\Pi^{-1}. \tag{48}$$

Then $\mathbf{X}$ in (33) and $\mathbf{X}_a$ in (40) can be rewritten as

$$\mathbf{X} = \Pi^{-1}\mathcal{P}\Pi^{-1} \quad \text{and } \mathbf{X}_a = \Pi^{-1}\mathcal{P}_a\Pi^{-1} \tag{49}$$

respectively. Let $\mathcal{N}(\cdot)$ denote the left null space of a matrix. It can be seen from (47) and (48) that $\mathcal{P}$ and $\mathcal{P}_a$ are two orthogonal projectors onto the left null spaces $\mathcal{N}(\mathbf{J}_2\Pi^{-1})$ and $\mathcal{N}(\mathbf{J}_{2a}\Pi^{-1})$, respectively (see [44, Sec. 5.13]). According to (41), the left null space $\mathcal{N}(\mathbf{J}_{2a}\Pi^{-1})$ is a subset of

$\mathcal{N}(\mathbf{J}_2\Pi^{-1})$, which implies $\mathcal{P}_a < \mathcal{P}$. Therefore, $\mathbf{X}_a \leq \mathbf{X}$ and $\mathbf{V} - \mathbf{J}_1\mathbf{X}_a\mathbf{J}_1^T \geq \mathbf{V} - \mathbf{J}_1\mathbf{X}\mathbf{J}_1^T$ according to (49). Then it can be concluded from (36) and (39) that $\mathbf{S}_f^a(\mathbf{S}_f^a)^T \geq \mathbf{S}_f\mathbf{S}_f^T$.

For the same reason as earlier, the left null space $\mathcal{N}(\mathbf{J}_{2a}\Pi^{-1})$ with more active inequality constraints in $\mathbf{J}_{2a}$ is a subset of $\mathcal{N}(\mathbf{J}_{2a}\Pi^{-1})$ with fewer active inequality constraints in $\mathbf{J}_{2a}$. Hence when more inequality constraints are active in solving the MHE problem, $\mathcal{P}_a$ becomes smaller, and fault sensitivity increases accordingly.

## REFERENCES


[1] P. Goupil, J. Boada-Bauxell, A. Marcos, P. Rosa, M. Kerr, and L. Dalbies, "An overview of the FP7 RECONFIGURE project: Industrial, scientific and technological objectives," *IFAC-PapersOnLine*, vol. 48, no. 21, pp. 976–981, 2015.

[2] R. Mehra, C. Rago, and S. Seereeram, "Autonomous failure detection, identification and fault-tolerant estimation with aerospace applications," in *Proc. Aerosp. Conf.*, Snowmass at Aspen, CO, USA, Mar. 1998, pp. 133–138.

[3] L. H. Mutuel and J. L. Speyer, "Fault-tolerant estimation," Ph.D. dissertation, Dept. Mech. Aerosp. Eng., Univ. California Los Angeles, Los Angeles, CA, USA, 2000.

[4] I. Rapoport and Y. Oshman, "Efficient fault tolerant estimation using the IMM methodology," *IEEE Trans. Aerosp. Electron. Syst.*, vol. 43, no. 2, pp. 492–508, Apr. 2007.

[5] C. Hajiyev and H. E. Soken, "Robust adaptive Kalman filter for estimation of UAV dynamics in the presence of sensor/actuator faults," *Aerosp. Sci. Technol.*, vol. 28, no. 1, pp. 376–383, 2013.

[6] Y. Gu, J. N. Gross, M. B. Rhudy, and K. Lassak, "A fault-tolerant multiple sensor fusion approach applied to UAV attitude estimation," *Int. J. Aerosp. Eng.*, vol. 2016, Jan. 2016, Art. no. 6217428, doi: 10.1155/2016/6217428.

[7] S. Timotheou, C. G. Panayiotou, and M. M. Polycarpou, "Moving horizon fault-tolerant traffic state estimation for the cell transmission model," in *Proc. 54th IEEE Conf. Decision Control*, Osaka, Japan, Dec. 2015, pp. 3451–3456.

[8] X. He, Z. Wang, L. Qin, and D. Zhou, "Active fault-tolerant control for an Internet-based networked three-tank system," *IEEE Trans. Control Syst. Technol.*, vol. 24, no. 6, pp. 2150–2157, Nov. 2016.

[9] X. He, Z. Wang, Y. Liu, L. Qin, and D. Zhou, "Fault-tolerant control for an Internet-based three-tank system: Accommodation to sensor bias faults," *IEEE Trans. Ind. Electron.*, vol. 64, no. 3, pp. 2266–2275, Mar. 2017.

[10] P. Castaldi, W. Geri, M. Bonfè, S. Simani, and M. Benini, "Design of residual generators and adaptive filters for the FDI of aircraft model sensors," *Control Eng. Pract.*, vol. 18, no. 5, pp. 449–459, 2010.

[11] P. Freeman, P. Seiler, and G. J. Balas, "Air data system fault modeling and detection," *Control Eng. Pract.*, vol. 21, no. 10, pp. 1290–1301, Oct. 2013.

[12] L. Garbarino, G. Zazzaro, N. Genito, G. Fasano, and D. Accardo, "Neural network based architecture for fault detection and isolation in air data systems," in *Proc. 32nd IEEE/AIAA Digit. Avion. Syst. Conf.*, East Syracuse, NY, USA, Oct. 2013, pp. 2D4-1–2D4-11.

[13] H. Alwi and C. Edwards, "Development and application of sliding mode LPV fault reconstruction schemes for the ADDSAFE benchmark," *Control Eng. Pract.*, vol. 31, pp. 148–170, Oct. 2014.

[14] H. Felemban, J. Che, C. Cao, and I. M. Gregory, "Estimation of airspeed using continuous polynomial adaptive estimator," in *Proc. AIAA Guid., Navigat., Control Conf.*, National Harbor, Maryland, 2014, pp. 1–8.

[15] D. Ossmann and H.-D. Joos, "Enhanced detection and isolation of angle of attack sensor faults," in *Proc. AIAA Guid., Navigat., Control Conf.*, San Diego, CA, USA, 2016, pp. 1–16, doi: 10.2514/6.2016-1135.

[16] M. B. Rhudy, M. L. Fravolini, Y. Gu, M. R. Napolitano, S. Gururajan, and H. Chao, "Aircraft model-independent airspeed estimation without pitot tube measurements," *IEEE Trans. Aerosp. Electron. Syst.*, vol. 51, no. 3, pp. 1980–1995, Jul. 2015.

[17] A. Cho, J. Kim, S. Lee, and C. Kee, "Wind estimation and airspeed calibration using a UAV with a single-antenna GPS receiver and pitot tube," *IEEE Trans. Aerosp. Electron. Syst.*, vol. 47, no. 1, pp. 109–117, Jan. 2011.

[18] S. Hansen and M. Blanke, "Diagnosis of airspeed measurement faults for unmanned aerial vehicles," *IEEE Trans. Aerosp. Electron. Syst.*, vol. 50, no. 1, pp. 224–239, Jan. 2014.

[19] T. A. Johansen, A. Cristofaro, K. Sørensen, J. M. Hansen, and T. I. Fossen, "On estimation of wind velocity, angle-of-attack and sideslip angle of small UAVs using standard sensors," in *Proc. Int. Conf. Unmanned Aircraft Syst.*, Denver, CO, USA, Jul. 2015, pp. 510–519.

[20] L. van Eykeren and Q. P. Chu, "Sensor fault detection and isolation for aircraft control systems by kinematic relations," *Control Eng. Pract.*, vol. 31., no. 10, pp. 200–210, Oct. 2014.

[21] P. Lu, E.-J. van Kampen, C. de Visser, and Q. Chu, "Nonlinear aircraft sensor fault reconstruction in the presence of disturbances validated by real flight data," *Control Eng. Pract.*, vol. 49, pp. 112–128, Apr. 2016.

[22] P. Tian, H. Chao, Y. Gu, and S. G. Hagerott, "UAV flight test evaluation of fusion algorithms for estimation of angle of attack and sideslip angle," in *Proc. AIAA Guid., Navigat., Control Conf.*, San Diego, CA, USA, 2016, p. 1.

[23] R. Avram, X. Zhang, J. Campbell, and J. Muse, "IMU sensor fault diagnosis and estimation for quadrotor UAVs," *IFAC-PapersOnline*, vol. 48, no. 1, pp. 380–385, 2015.

[24] J. Marzat, H. Piet-Lahanier, F. Damongeot, and E. Walter, "Model-based fault diagnosis for aerospace systems: A survey," *Proc. Inst. Mech. Eng., G, J. Aerosp. Eng.*, vol. 226, no. 10, pp. 1329–1360, 2012.

[25] Q. Shen, B. Jiang, and V. Cocquempot, "Fault diagnosis and estimation for near-space hypersonic vehicle with sensor faults," *Proc. Inst. Mech. Eng., I, J. Syst. Control Eng.*, vol. 226, no. 3, pp. 302–313, 2012.

[26] D. Briere and P. Traverse, "AIRBUS A320/A330/A340 electrical flight controls—A family of fault-tolerant systems," in *23rd Int. Symp. Fault-Tolerant Comput. Dig. Papers*, Toulouse, France, Jun. 1993, pp. 616–623.

[27] V. Fernández *et al.*, "A tool for industrial verification and benchmarking of FDD/FTC designs," *IFAC-PapersOnLine*, vol. 48, no. 21, pp. 1006–1011, 2015.

[28] Y. Wan, T. Keviczky, and M. Verhaegen, "Robust air data sensor fault diagnosis with enhanced fault sensitivity using moving horizon estimation," in *Proc. Amer. Control Conf.*, Boston, MA, USA, Jul. 2016, pp. 5969–5975.

[29] Y. Wan and T. Keviczky, "Implementation of real-time moving horizon estimation for robust air data sensor fault diagnosis in the RECONFIGURE benchmark," *IFAC-PapersOnLine*, vol. 49, no. 17, pp. 64–69, 2016.

[30] S. S. Mulgund and R. F. Stengel, "Optimal nonlinear estimation for aircraft flight control in wind shear," *Automatica*, vol. 32, no. 1, pp. 3–13, 1996.

[31] J. W. Langelaan, N. Alley, and J. Neidhoefer, "Wind field estimation for small unmanned aerial vehicles," *J. Guid., Control, Dyn.*, vol. 34, no. 4, pp. 1016–1030, 2011.

[32] B. L. Stevens and F. L. Lewis, *Aircraft Control and Simulation*. Hoboken, NJ, USA: Wiley, 1992.

[33] M. Davies, *The Standard Handbook for Aeronautical and Astronautical Engineers*. New York, NY, USA: McGraw-Hill, 2003.

[34] G. Hardier, C. Seren, P. Ezerzere, and G. Puyou, "Aerodynamic model inversion for virtual sensing of longitudinal flight parameters," in *Proc. Conf. Control Fault-Tolerant Syst.*, Nice, France, 2013, pp. 140–145.

[35] C. V. Rao, J. B. Rawlings, and D. Q. Mayne, "Constrained state estimation for nonlinear discrete-time systems: Stability and moving horizon approximations," *IEEE Trans. Autom. Control*, vol. 48, no. 2, pp. 246–258, Feb. 2003.

[36] J. B. Rawlings and B. R. Bakshi, "Particle filtering and moving horizon estimation," *Comput. Chem. Eng.*, vol. 30, nos. 10–12, pp. 1529–1541, Sep. 2006.

[37] A. Alessandri, M. Baglietto, and G. Battistelli, "Moving-horizon state estimation for nonlinear discrete-time systems: New stability results and approximation schemes," *Automatica*, vol. 44, no. 7, pp. 1753–1765, Jul. 2008.

[38] D. Sui and T. A. Johansen, "Moving horizon observer with regularisation for detectable systems without persistence of excitation," *Int. J. Control*, vol. 84, no. 6, pp. 1041–1054, 2011.

[39] J. Nocedal and S. J. Wright, *Numerical Optimization*, 2nd ed. New York, NY, USA: Springer, 2006.

[40] P. Kühl, M. Diehl, T. Kraus, J. P. Schlöder, and H. G. Bock, "A real-time algorithm for moving horizon state and parameter estimation," *Comput. Chem. Eng.*, vol. 35, no. 1, pp. 71–83, Jan. 2011.

[41] B. M. Bell, J. V. Burke, and G. Pillonetto, "An inequality constrained nonlinear Kalman–Bucy smoother by interior point likelihood maximization," *Automatica*, vol. 45, no. 1, pp. 25–33, 2009.

[42] N. Haverbeke, "Efficient numerical methods for moving horizon estimation," Ph.D. dissertation, Katholieke Univ. Leuven, Leuven, Belgium, 2011.

[43] S. X. Ding, *Model-Based Fault Diagnosis Techniques: Design Schemes, Algorithms, and Tools*, 2nd ed. London, U.K.: Springer-Verlag, 2013.
[44] C. D. Meyer, *Matrix Analysis and Applied Linear Algebra*. Philadelphia, PA, USA: SIAM, 2000.

**Yiming Wan** received the Ph.D. degree in systems and control from Tsinghua University, Beijing, China, in 2013.

From 2013 to 2016, he was a Post-Doctoral Researcher with the Delft Center for Systems and Control, Delft University of Technology, Delft, The Netherlands. He is currently a Post-Doctoral Associate with the Massachusetts Institute of Technology, Cambridge, MA, USA, and will be an Associate Professor with the School of Automation, Huazhong University of Science and Technology, Wuhan, China. His current research interests include model-based and data-driven fault diagnosis and fault-tolerant control.

**Tamás Keviczky** received the M.S. degree in electrical engineering from the Budapest University of Technology and Economics, Budapest, Hungary, in 2001, and the Ph.D. degree from the Control Science and Dynamical Systems Center, University of Minnesota, Minneapolis, MN, USA, in 2005.

He was a Research Intern with Honeywell Laboratories, Minneapolis, MN, USA, and a Post-Doctoral Scholar with the Control and Dynamical Systems, California Institute of Technology, Pasadena, CA, USA. He is currently an Associate Professor with the Delft Center for Systems and Control, Delft University of Technology, Delft, The Netherlands. His current research interests include distributed and embedded optimization for optimal control, model predictive control, fault-tolerant control, and distributed control and estimation of large-scale systems with applications in aerospace, automotive, mobile robotics, industrial processes, and infrastructure systems such as water and power networks.

Dr. Keviczky was a co-recipient of the AACC O. Hugo Schuck Best Paper Award for Practice in 2005.